Progress in Aerospace Sciences xxx (xxxx) xxxx

Contents lists available at ScienceDirect

Progress in Aerospace Sciences

journal homepage: www.elsevier.com/locate/paerosci

Review of measurement techniques for unsteady helicopter rotor flows

A.D. Gardner*, C.C. Wolf, M. Raffel

German Aerospace Center (DLR), Göttingen, Germany

ARTICLE INFO

Keywords:
Unsteady flow
Measurement techniques
Helicopter rotors
Pressure transducer
PSP
Boundary layer transition
Hot-film anemometry
TSP
DIT
IR thermography
Dynamic stall
PIV
BOS
Vortex

MSC:
2010 MSC: 76-02
76-05

ABSTRACT

The helicopter group at the DLR in Göttingen has been actively involved in the development of measurement techniques for unsteady flows, particularly as they apply to the problems found in unsteady rotor blade aerodynamics. This includes the development and validation of new techniques for the detection of dynamically moving boundary layer transition, and for the detection of dynamic stall and other transient flow separation events. These new techniques include pressure sensor analysis, differential infrared thermography, local infrared thermography and the automated analysis of hot-film data. Particle image velocimetry (PIV) and background oriented schlieren (BOS) have been used for the analysis of the unsteady off-body flow, and synchronised PIV-BOS-pressure measurements have allowed direct comparisons between different methods. The Lagrangian volumetric PIV variant, shake-the-box, has been used to analyse secondary vortex structures in the vortex wake.

This review article will give an overview of the advances in that group, as well as placing their activities in the context of international advances in these areas.

1. Introduction

The main rotor blade of a helicopter in forward flight exhibits unsteady flow with a primary rotation period of the order of 1–10 Hz and pulse phenomena (for example Blade-Vortex Interaction (BVI), Dynamic Stall (DS), or Shock-Buffet) with time constants requiring acquisition frequencies in the range 500 Hz-10 kHz. As such the aerodynamic phenomena seen on the helicopter rotor blade lie within the modern rage of scientific visible light and infrared cameras, high-speed lasers, and well below the upper limits of pressure sensors and hot-film anemometers. This means that the data-gathering part of techniques like Particle Image Velocimetry (PIV), Background-Oriented Schlieren (BOS) and infrared thermography (IRT) is possible, and pressure and hot-film data can also be acquired. The measurement of unsteady aerodynamic phenomena is subject to a range of critical difficulties which are not present for static phenomena. Particularly the data analysis presents significant challenges to recover meaningful aerodynamic data from the measurements. Additional challenges compared to static flows are the reduced number of samples available for averaging to reduce noise, the effect of aperiodicity and vortex wandering, and the handling of inertia, synchronisation and lag in the measurements. However unsteady flows offer a significant expansion of the possible palette of instantaneous aerodynamic situations, and a range of new and interesting phenomena, which makes unsteady flows an exciting field to measure and analyse.

This paper includes an overview of the work in unsteady measurement techniques in the helicopter aerodynamics group at the DLR in Göttingen over the last 10 years. This group develops methods of aerodynamic analysis for rotary wing applications using experimental and numerical tools, and has had an average of 3–4 full-time employees and 3–5 doctoral students during the last decade. The German Aerospace center (DLR), is a primarily publicly funded research organisation with around 8000 employees, with research interests in the fields of air travel, ground vehicles, space travel and energy.

2. Unsteady aerodynamics test cases

The work of the helicopter aerodynamics group in Göttingen has

* Corresponding author.
E-mail address: tony.gardner@dlr.de (A.D. Gardner).

https://doi.org/10.1016/j.paerosci.2019.100566
Received 27 June 2019; Received in revised form 14 August 2019; Accepted 15 August 2019

List of abbreviations

1D/2D/3D	1/2/3 Dimensional
BOS	Background-Oriented Schlieren
BVI	Blade-Vortex Interaction
CFD	Computational Fluid Dynamics
DEHS	Mineral oil for PIV seeding
DIT	Differential Infrared Thermography
DLR	German aerospace center
DMD	Dynamic Mode Decomposition
DS	Dynamic Stall
FOV	Field of View
HF	Hot film gauges
IR	Infrared
IRT	Infrared Thermography
LDV	Laser Doppler Velocimetry
LIT	Local Infrared Thermography
PIV	Particle Image Velocimetry
POD	Proper Orthogonal Decomposition
PSP	Pressure Sensitive Paint
PtTFPP	platinum tetra(pentafluorophenyl) porphyrin
(U)RANS	(Unsteady) Reynolds-Averaged Navier-Stokes
RTG	Rotor Test stand Göttingen
SPR	Stereo Pattern Recognition
STB	Shake-the-Box
TSP	Temperature Sensitive Paint
UV-LED	Ultraviolet light source

List of Symbols

α, β	Geometric angle of attack
C_f	Skin friction coefficient
Δ	Difference between signals
f	Frequency (Hz)
Γ	Circulation
I	Intensity of optical signal
M	Mach number
ψ	Azimuthal angle
P, C_p	Pressure (Pa), Pressure coefficient
σC_p	Standard deviation of pressure signal
r/R	Radial position normalised with rotor radius
t/T, Θ, $f \times t$	Position in Phase
T	Temperature (K)
V	Flow velocity
x,y,z	Linear dimensions
x/c, y/c	Chordwise position, spanwise position normalised with airfoil chord

focused on the study of aerodynamically analogous test cases, which are relevant for helicopter aerodynamics. Older work focused on the airfoil with prescribed sinusoidal or other pitching movement [1–3], see Fig. 1a, which is analogous to parts of the helicopter rotor rotation cycle with low sweep ($\Psi = 90^{\circ}$ and $\Psi = 270^{\circ}$). These test cases were used to calibrate 2D computational fluid dynamics (CFD) codes and develop dynamic stall modelling [4]. It was noted that the wind tunnel experiments, which had an aspect ratio of 3.3:1, produced lower stall peaks and less concentrated vortices than the 2D simulations, and the reason was the presence of three dimensional flow. For that reason, in recent times the pitching airfoil has primarily been used as a test bed for investigating flow control [5,6] and new measurement techniques [7,8]. For the nominally 2D airfoil the 3D flow is caused by an interaction between the airfoil and the wind tunnel sidewall, which was demonstrated using CFD and pressure measurements for static angles of attack [9]. The interaction was observed for dynamic stall test cases with a pitching airfoil using pressure sensitive paint, showing that a strongly 3D flow was generated on the nominally 2D geometry [10].

The 2D pitching airfoil was thus succeeded by two alternatives: The pitching finite wing [11,12], and the rotor with axial inflow [13]. The pitching finite wing, see Fig. 1b, was prepared with a positive twist toward the blade tip, resulting in a considerable reduction in the sidewall interference effect, compared with the nominally 2D airfoil, and in fact better 2D flow and boundary layer transition than the "2D" test case [14]. The finite pitching wing was investigated for three aerodynamic phenomena: dynamic stall, tip vortex and boundary layer transition. It could be shown that a 3D dynamic stall with an omega vortex was generated, which is comparable to that seen for more complex test cases [11]. The dynamic stall could be well predicted using 2nd order RANS computations with a sufficiently fine grid and errors in the numerical prediction were primarily confined to errors in the phase (or timing) of stall events, when compared with the experiments [15]. Although the differences were larger than for fully attached flow, the high quality of both the experiments and the CFD to the setup resulted in acceptable qualitative and quantitative agreement for all test cases considered. The tip vortex for the dynamic pitching test case showed an interesting jetting phenomenon associated with lift breakdown on the wing, but for the attached flow the results were as expected [16,17]. Unexpectedly, the finite wing had an experimental disadvantage in that the wake preservation to large ages would have required a much longer test section than was available. This problem was better addressed by the rotor with axial inflow.

The rotor with axial inflow is an aerodynamic experiment for unsteady flow in a rotating system [13]. The RTG rotor produces unsteady flow by using large cyclic pitch together with an axial inflow and includes some influences of centrifugal and Coriolis forces. The flow field

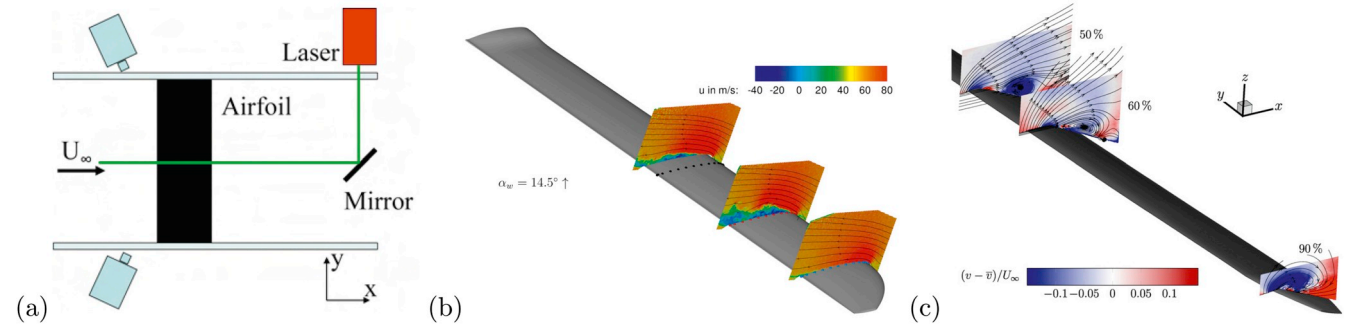

Fig. 1. Unsteady aerodynamic test cases, (a) Stereo high-speed PIV setup on a pitching airfoil, from Ref. [3], (b) Pitching finite wing with high-speed PIV results, from Ref. [12] (c) Rotor in forward flight in a wind tunnel with low-speed PIV [23]. The experimental complexity and the comparability to flight is increased from left to right.

is not the same as in edgewise dynamic stall due to the missing wake generation and Mach number variation, however relevant high-quality validation data can be generated in the laboratory at a fraction of the cost of a forward-flight wind tunnel experiment. This is particularly important for the investigation of blade tip vortices since in contrast to the wing tip vortices of fixed-wing aircraft, rotor vortices experience a flow normal to the axial direction which promotes vortex decay, and the vortices are produced with a curvature which also promotes vortex decay [18]. The rotor can be operated with cyclic pitch, meaning that the rotor blade changes its geometric angle of attack as a function of azimuthal position, performing a pitching cycle once per revolution in a similar fashion to the pitching airfoil. The tip vortex then trails the rotor in a helical path and vortex breakdown in a function of the load and induced fluctuations on the vortex [19]. The boundary layer transition is primarily a function of the 2D flow, but in contrast to the pitching wing, the measurement of the local aerodynamic angle of attack is complex, and it can be significantly different to the geometric angle of attack [20].

Finally, the measurements of model-scale [21], and full-scale [22] helicopters in free flight with high-speed PIV and BOS allows the tracking of flow features, and the verification that the effects seen in simplified laboratory experiments actually occur on the helicopters of interest. The difficulty of the measurements increases and the quality of data reduces with the move from nonrotating to rotating test cases, and again with the move from laboratory test-beds [23], see Fig. 1c, to free flight, but the relevance of the measurements is improved.

3. Unsteady pressure measurement

3.1. Pressure sensors

The pressure sensors used in the investigations in Göttingen are two different high-speed miniature pressure sensors from the firm Kulite, operating on the strain gauge principle with a full bridge. The pressure taps are small holes of 0.2–0.3 mm diameter in the surface of the airfoil, see Ref. [24]. The depth of the pressure tap in the surface is 1 mm, with a larger diameter tube (0.6 mm) attached to the back of the surface, see Fig. 2. After a length of 5 mm–40 mm (depending on the specific geometry of the wind tunnel model), the pressure transducer is mounted. The sensor found to have good performance and excellent long-term stability (>10 years without significant degradation) is the Kulite XCQ093 miniature pressure sensor. Where insufficient space is available to mount this sensor, Kulite LQ-062 sensors were used, see Fig. 3, but this sensor showed up to 30% sensor losses in the integration and initial testing phases. The sensors are fully calibrated (generally using 10–20 pressure calibration levels covering the expected pressure range), at multiple points in each test, since it is assumed that the calibration changes depending on the local stresses on the sensor. In fact it has been noted that after the initial integration, the calibrations are similar enough to be compensated with a zero-point offset, and that a significant change (>5%) in the calibration is exclusively an indication of sensor failure.

The internal geometry of the pressure tap and sensor mountings for each test are computed for their reaction to a pressure step of 30%, using a 1D Navier-Stokes solver of the internal tubing (DLR-internal code Kryodiff). It is assumed that the steps observed during the experiments are not susceptible to a small perturbation frequency and time correction, and thus direct data analysis is used. The sensor mountings are considered to be acceptable when all sensors succeed in transmitting 99% of this pressure step in 1/2000 s. A typical sampling rate for large models is 6 kHz, with an anti-aliasing filter at 3 kHz, and for small models sampling at 20 kHz with an anti-aliasing filter at 10 kHz is used. Comparisons with external sensors indicate that for small test perturbations that the pressure sensors are accurate to 10 k Hz. The Kulite sensors themselves have much higher resonant frequencies so that the limitations are due to the mounting systems.

The pressure sensor positioning follows two different strategies. For larger models, for example the 2D airfoils in Refs. [2,25] sufficient space is available that a large number of pressure sensors (generally about 50) can be installed underneath the airfoil surface. The airfoils are constructed of two carbon-fiber half-shells, an aluminium spar and aluminium mounting feet, which are instrumented while open, and then glued closed, see Fig. 4. The pressure sensors are installed near the centerline at an angle of 10° to the oncoming flow to reduce wake interference from the preceding pressure taps. The pressure sensor distributions are designed using CFD computations of all expected Mach and Reynolds numbers, angles of attack and unsteady pitching conditions. A linear interpolation of the pressures from the pressure transducers [26] is analysed (Fig. 5) and the pressure sensors are clustered in regions of high pressure gradient to reduce the error in C_L, C_D and C_M to less than 1% of the peak value, see Ref. [27]. Despite this, it is always expected that any comparison with CFD will require reducing the computed pressure distributions to only the positions which were available in the experiment, for example as [4,15]. This is particularly necessary if any of the pressure sensors of the original design are non-functional during the wind tunnel test.

The second method of pressure sensor positioning is used when technical considerations including available space inside the aerodynamic model does not permit the use of fully defined pressure cuts. For example in the small rotor blades of the Rotor test stand Göttingen (RTG) [13], only 10 sensor positions were instrumented, see Fig. 3, of which only seven were functional during the experiment. As shown by Ref. [28], the linear integration of the pressure transducer data can lead to a qualitatively similar dynamic force history, but this is by no means guaranteed. An alternative method is to match the measured pressure distributions with computed pressure distributions using a least-squares search and then use the computed pressure distributions for further investigations. As shown by Weiss et al. [20], this allows a complex analysis of n-factor amplification, for instance, or equally, the dynamic boundary layer transition behaviour can also be compared [29]. Under resolved pressure distributions must be treated with some care, as the integration can result in qualitatively unexpected results, including oscillations which would not be present in a more finely resolved measurement [30].

In recent years airfoil data was acquired using a Dewetron digital data recorder, and all channels are acquired with the same time-scale. The data recorder is timed so that the sampling rate is fixed to the airfoil pitching rate, and 1024 samples are acquired per pitching period (i.e. 6144 Hz for pitching at 6 Hz). To allow the convergence of averaging, 160 periods of data are acquired, for a total measurement time which varies with the airfoil pitching rate (27 s for 6 Hz pitching). After the data has been acquired, it is archived together with all of the wind tunnel data including wall shape and flow conditions.

Each of the data points is typically phase-averaged for a mean and standard deviation of C_P, C_L, C_D and C_M. The mean is used for comparison with CFD and between different measurement points, and the standard deviation gives a measure of the cycle-to-cycle variation. Cycle-to-cycle variations come from structural vibrations and

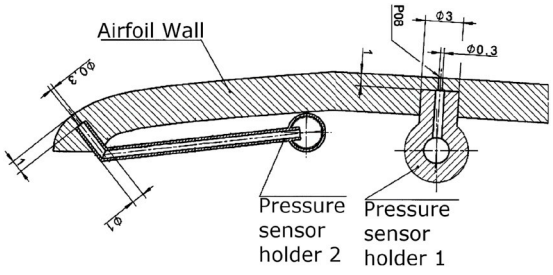

Fig. 2. Kulite sensor installation, from Ref. [24]. The sensors are installed in holders and connected by tubes to the underside of the composite shell.

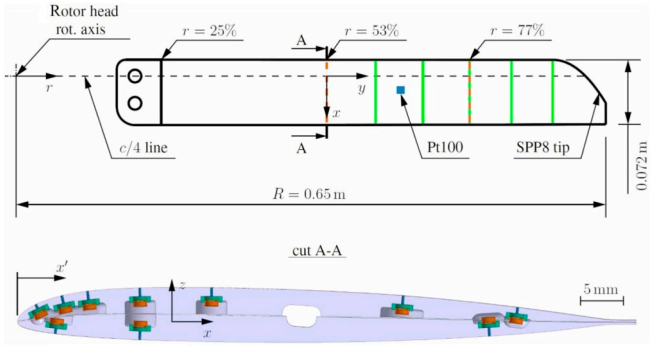

Fig. 3. Instrumentation on the RTG rotor blade, from Ref. [13]. Two pressure sensor sections (r/R = 0.53 and 0.77), PT100s and five PIV measurement planes are used.

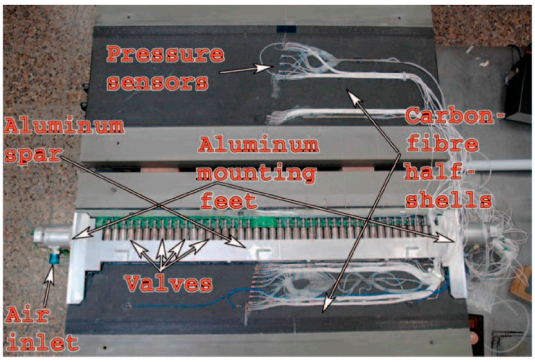

Fig. 4. Instrumented airfoil model before closing, from Ref. [25]. This is a flow control model including ports and valves for pulsed blowing, as well as 48 Kulite pressure sensors in one cut. Blue wires indicate accelerometers and PT100 temperature sensors for monitoring the model. (For interpretation of the references to colour in this figure legend, the reader is referred to the Web version of this article.)

turbulence or separated flow. Thus for each angle of attack on the upstroke and each on the downstroke a pressure distribution and set of forces is available. This results in accurate results for many test cases, particularly at higher Mach numbers [2,25], but for many lower Mach numbers or other airfoils, phase averaging results in significant errors in the estimation of peak forces, for instance, see Ref. [31]. For many cases, this problem can be addressed by using the average-of-peaks rather than the peak-of-average, so that the error in the peak is specifically statistically addressed, see Ref. [11], and with this method, a good comparability to CFD is achieved [15]. The phase averaging of the data additionally allows the detection of the dynamic movement of the boundary layer transition position, as addressed later in this paper, see Ref. [24].

The repeatability of nominally identical points measured on different days can be used as a substitute for error. For simple models with attached flow the repeatability of C_L is better than 1%, and the repeatability of C_D, and C_M, is within 3% for nominally identical test points. The systematic errors due to the wind tunnel blockage and sidewall effect can be corrected for steady tests, but for unsteady tests no reliable correction method for the wind tunnel effects is known, and the data is mainly analysed in an uncorrected form.

3.2. Pressure sensitive paint

The pressure sensitive paint (PSP) technique uses photokinetic interactions to measure the partial pressure of oxygen at a surface using an applied florescent coating, see Bell et al. [32] and Liu and Sullivan [33]. Excitation light at short wavelengths is absorbed by the light-sensitive luminophores, and the dye molecules emit light at longer wavelengths. The amount of florescent emission is reduced by oxygen diffused into the surface, the amount of which depends on the local air pressure. Higher local pressure reduces both the amount of light emitted as well as the luminescent lifetime decay time.

High speed pressure sensitive paint is becoming increasingly applicable to helicopter applications. In addition to results on a pitching airfoil [10], and on the RTG rotor [34], several groups have reported results for a rotor in hover and forward flight [35], high-speed rotating blade in hover [36], and for rotating blades and pitching airfoils [37]. The pressure-sensitive paint used in Göttingen is a platinum tetra (pentafluorophenyl) porphyrin (PtTFPP) based PSP in combination with a styrene-based polymer, and was developed by the DLR in co-operation with the Organic-Chemistry Institute of the University of Hohenheim, Germany [38]. The porosity of this paint was enlarged by adding TiO_2 powder, and the paint was applied with a spray gun to the model surface, either without an additional screen layer underneath, or with a white screen layer which results in higher signal intensity. The paint can be applied in-situ in the wind tunnel, and is water-washable for removal. A total paint thickness of 10 ± 2 µm without the screen layer is typical. Unsteady PSP has a relatively high temperature sensitivity on the order of − 800 Pa/°C.

A constant UV-LED illumination can be used together with the intensity method, see Refs. [39,40], or a laser illumination with the lifetime method, see Ref. [34], to acquire luminosity images from a visible-light camera with a band-pass filter. The paint emits light and the light intensity (brightness) is a function of pressure, paint application, illumination and observation angle. Reference images taken at flow-off conditions must be used to reference the paint application, illumination and observation angle data, and thus the intensity of the measurement images remain only a function of pressure. The measurement images are then mapped onto a 3D volume using marker tracking and calibration data applied to convert light intensity to pressure.

Both “in-situ” and “a-priori” calibrations are performed. Generally,

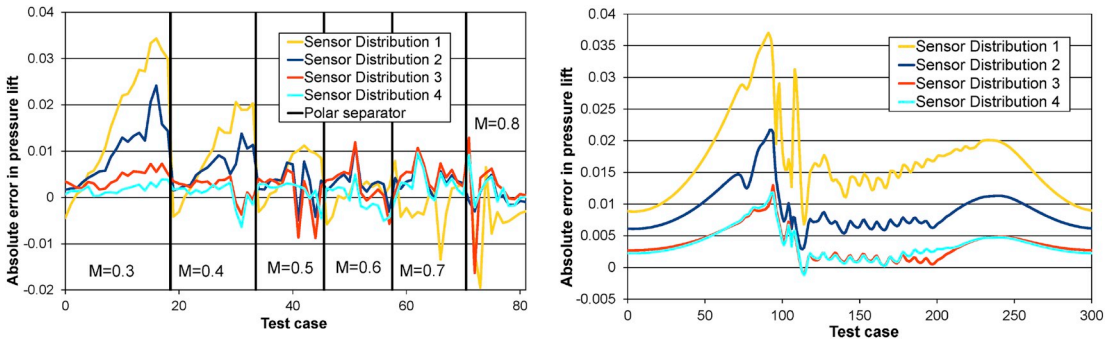

Fig. 5. Pressure distribution design for large numbers of pressure transducers. Left: Static polar test cases, Right: Dynamic stall test case, from Ref. [27]. Each line shows the differing accuracy when the pressure distribution is changed, and the different lines are different sensor arrangements for the same number (50) of sensors.

for 25°C the in-situ calibration and the a-priori calibration have good agreement and the a-priori calibration is used for the final data reduction. The PSP data requires a zero-offset from an adjacent pressure transducer. When this is performed the PSP and pressure transducer signals follow each other well, as shown in Fig. 6, with some aliasing due to the differing sampling rates of the two data sets. The PSP data requires a zero-offset from an adjacent pressure transducer. When this is performed the PSP and pressure transducer signals follow each other well, as shown in Fig. 6, with some aliasing due to the differing sampling rates of the two data sets. The pressure transducers were sampled at 5878 Hz with an anti-aliasing filter at 3 kHz. The PSP data was sampled at 367 Hz and the sampling was phase locked so that this was equivalent to 1024 and 64 points per pitching period, respectively.

Pressure sensitive paint has been particularly useful where the topography of separating flow is difficult to measure, as in the pitching airfoil undergoing dynamic stall in Fig. 7. Here the model centerline is at the bottom of the images, and the wind tunnel sidewall is at the top of the images. The low pressure in the dynamic stall vortex causes the footprint of the vortex on the surface to be green in the images. The interaction with the wind tunnel wall causes the dynamic stall vortex to become bowed and strongly 3D. A rapidly moving rotor blade in hover is an unsteady object which nonetheless has a static flow in the blade reference system, and this could be frozen using the lifetime method, see Fig. 8. Here the sparse pressure instrumentation of the rotor blade, described in the previous section and shown in Fig. 3, is significantly augmented by the use of pressure sensitive paint.

A particular challenge for PSP measurements on fast rotating blades is the balance between short exposures to reduce blur and longer exposures to increase signal. Accumulating a large number of phase-locked exposures has worked for stiff objects including fans (Bencic [41]), turbocharger compressors (Gregory [42]), turbine rotors (Suryanarayanan et al. [43]) and propellers (Klein et al. [44]). However due to lower harmonic resonance in lag and flapping, helicopter rotor blades do not produce a truly periodic flow of the type needed to use this method, see Wong et al. [45,46]. These limitations are overcome by using the single-shot lifetime technique as employed by Juliano et al. [47], and Disotell et al. [48], who applied the method for unsteady PSP measurements on a small-scale fully articulated helicopter blade in forward flight. The technique has recently matured to be used on wind tunnel helicopter blades in forward flight (Watkins et al. [49]).

4. Unsteady boundary layer transition measurement

A number of significant advances in unsteady boundary layer transition point measurement have been made by the helicopter group in Göttingen. Although boundary layer transition measurement is not new, see for instance Refs. [50,51] for hot-film measurements on a pitching finite wing, or indeed for a helicopter rotor blade [52], experiments in this area have historically been suboptimal for use as CFD code calibration. Firstly, the definition of a “transition point”, while numerically attractive, is marred by the finite length of the transition region in the flow direction [53]. The dimension between the end of laminar flow and the start of turbulent flow can easily exceed 10% chord in the suction side of a helicopter airfoil, and can approach 50% of the chord length on the pressure side of a helicopter airfoil [54]. Secondly, the definition of “transition point” varies widely in the literature between transition start, end and 50% intermittency (or maximal C_f or heat flux gradient), both in experimental and numerical investigations. Thirdly, low data density and difficulties in the data analysis have often produced data which is not of sufficient “quality” for CFD calibration, although the paucity of available data increases its value considerably [55,56]. Finally, advances in automated data analysis mean that the large amount of data produced by hot-film or optical methods can be algorithmically evaluated, rather than relying on hand-analysis of a few selected points [8,57]. Thus recent years have seen a significant increase in the number and quality of unsteady data sets available for CFD validation, which also allows advances in that area [29].

4.1. Hot-film gauges

Hot-film gauges use a thin metallic sensor which is deposited onto a thermally and electrically insulating surface. The sensor is heated electrically and the heat flux from the sensor into the flow is a function of the wall shear stress. The hot-film anemometers are operated in constant-temperature mode, requiring complex electronics to balance the heat-loss from the flow, and the voltage signal is proportional to the wall heat flux. Limiting frequencies are between 20 kHz and 50 kHz, depending on the precise experimental arrangement. The hot-film gauges are not calibrated, and the changes in the signal over time are used to make statements about the boundary layer state, see Fig. 9. In contrast to other methods of transition detection, hot-film gauges can also detect flow separation, and they are the method of choice for boundary layer transition measurements where possible. Unfortunately, the experimental effort and cost of installing hot-film gauges is often prohibitive, and the operation of the gauges requires personnel with specific training.

Richter et al. [53] shows a typical airfoil with hot-film setup, see Fig. 10. The airfoil was additionally equipped with hot film sensors deposited onto two Kapton sheets. The sensors were placed on a line with an inclination of 15° to the main flow direction to reduce the passage of a sensor's wake over other sensors. The sheets were glued onto the model in specially prepared recesses, so that no thickness was added to the model, and the edges were carefully filled and smoothed to prevent disturbances in the flow. The electrical wiring was installed inside the model. The hot film sensor arrays consisted of nickel sensor elements and copper leads. The sensor elements had a length of 1.4 mm, a width of 0.1 mm, and a height of 0.2 μm. The nominal cold resistance of the sensor element was 9–10 Ω. The copper leads had a width of 3 mm, height of 4.2 μm, and various lengths due to the layout of the array, with a maximum resistance of 1.4 Ω. Hot film data were sampled at f = 120 kHz and synchronised with the pressure measurements (f = 6758 Hz). Both the hot film and the pressure data were recorded for 160 pitching periods of the model.

Automated data analysis for the hot-film data [57] uses the zero passing points of the statistical skewness to detect the beginning, 50% intermittency and end of transition as the boundary layer transition position moves over each sensor in time. This algorithm provides results which are identical to transition positions detected using voltage peaks, derivative or kurtosis, but is more robust against experimental noise and is thus better for automated transition detection algorithms. The

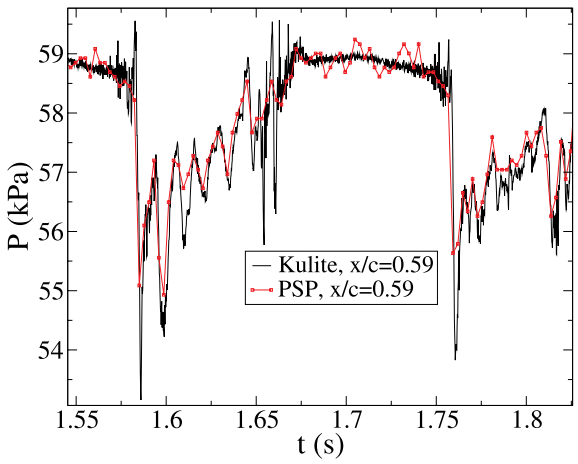

Fig. 6. Model pressure comparison over time for a single pressure transducer and a PSP point, from Ref. [10].

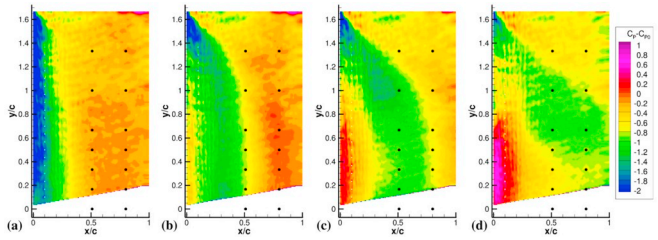

Fig. 7. Pitching airfoil undergoing dynamic stall, from Ref. [10]. Time advances from left to right. The PSP shows the decay of the suction peak (blue) followed by the development of a dynamic stall vortex with a suction footprint (green) on the airfoil surface. The dynamic stall vortex is strongly curved from the wind tunnel midline (bottom) and remains at the airfoil leading edge near the wind tunnel wall (top). (For interpretation of the references to colour in this figure legend, the reader is referred to the Web version of this article.)

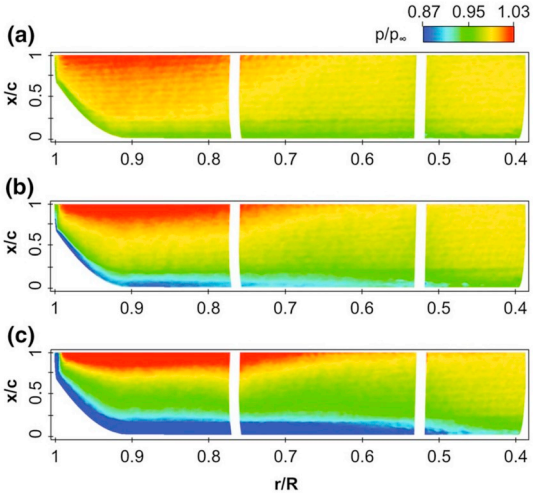

Fig. 8. PSP surface pressures on the RTG rotor. Static root angle 17° for different rotation rates f = (a) 24 Hz, (b) 35 Hz, (c) 47 Hz, from Ref. [34].

Fig. 10. Airfoil with hot-films, from Ref. [53]. The pitching airfoil is driven by shafts at the x/c = 0.25 position and 50 Kulite pressure transducers were included.

boundary layer transition position detected by hot-films in this way has been compared to other methods [58], and it has been found that the mounting surface is the main source of systematic error, both due to the change in surface roughness over the Kapton sheet compared to the airfoil surface, and due to the shape change of the airfoil near the leading edge after installation and edge filling of the Kapton sheet.

4.2. Unsteady boundary layer transition measurement using pressure sensors

In contrast to hot-film sensors, a larger number of wind tunnel models are instrumented with pressure sensors as standard. The pressure signals can be analysed to produce boundary layer transition positions for both static and varying flows, although the method works best for dynamically periodic flow [24]. The method has been demonstrated for test cases with dynamic pressure sensors mounted in the model, see Figs. 2 and 3, but it does not rely on a high-frequency response, rather on broadband signal, and works for static cases even with a low-pass filter at 1 Hz. The method detects the 50% intermittency position, but cannot detect the start and end of transition, and the

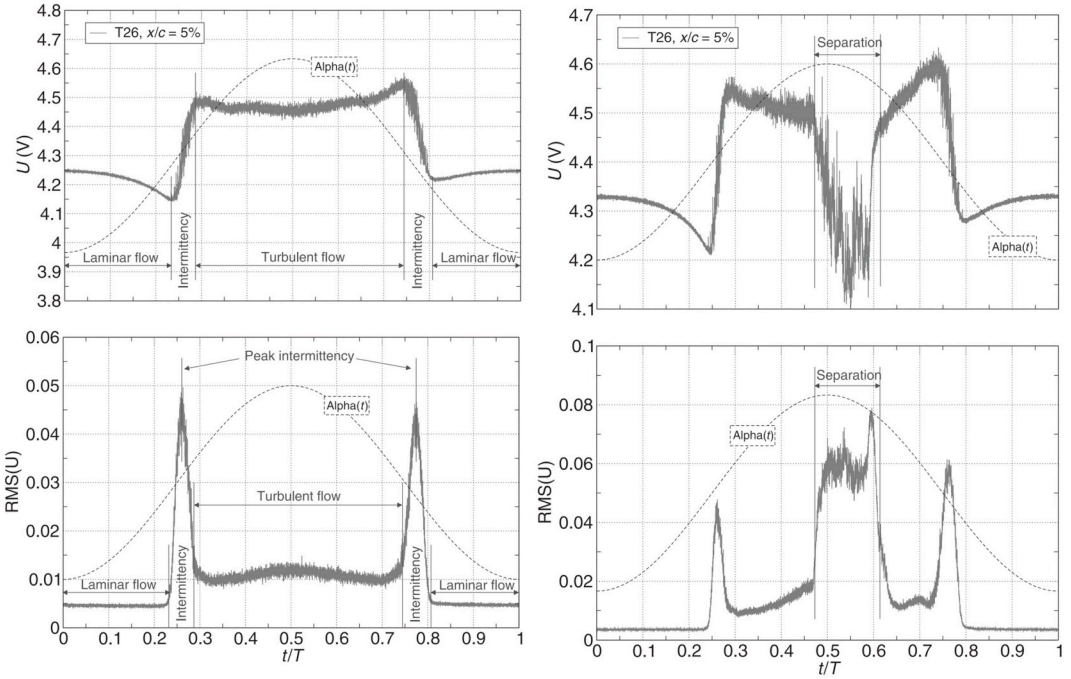

Fig. 9. Hot-film data analysis for a pitching airfoil, from Ref. [53]. The passage of the laminar-turbulent transition over the sensor is visible as both a step in the absolute voltage and a peak in the voltage RMS. Flow separation can be distinguished from boundary layer transition.

presence of shocks or flow separation is only acceptable if there is a physical or time separation between these effects and boundary layer transition.

When the boundary layer transitions from laminar to turbulent, the displacement thickness, δ, of the boundary layer undergoes a rapid thickening, which can also be used directly to detect transition [59]. This thickening is experienced by the outer flow as a kink outwards from the wall, which increases the acceleration of a subsonic flow compared to the closely surrounding regions without boundary layer transition. The statistical turbulence leading to the transition results in an amplification of the low turbulence present in the outer flow, so that the transition position experiences a constant slight movement with a broadband signature. For a pressure sensor directly under the displacement thickness kink, the variance in the pressure signal is significantly increased compared to neighbouring positions, since the pressure gradient $\Delta P/\Delta x$ is high at that position. By finding the peak in the standard deviation of the pressure coefficient, σC_P, the transition position can be found, and this has been validated against hot-film and infrared data [24,58]. The low spatial discretisation compared to the high time discretisation of the pressure signals mean that the transition position detection works best when the transition position is moving over the pressure sensor position, see Fig. 11.

In addition to the original measurements, transition detection using σC_P has been used for a finite wing, with higher flexibility than an airfoil [11,14], and on a stiff rotor with axial inflow [13,60]. It has not yet been demonstrated for pressure measurements using long tubes, although that should be possible, or for a flexible rotor in forward flight. The detection of boundary layer transition using the pressure sensors is subject to a systematic bias of the boundary layer transition upstream for cases where the holes of the pressure taps act as an increased wall roughness [8,61], and for dynamic flow the effect of the increased wall roughness is to accelerate the upstream movement of the boundary layer transition, while the downstream movement is relatively unaffected [62].

4.3. Differential infrared thermography and local infrared thermography

Differential infrared thermography (DIT) is an approach to the analysis of infrared thermography (IRT) images, particularly those taken using the high-speed infrared cameras which have recently become available for scientific purposes. These cameras have short integration times (50–200μs) and fast image repetition (100 Hz–1000 Hz). Classical infrared imaging [63,64] suffers from the problem that the surface temperature takes very long times (up to 10 min) to come into thermal equilibrium with the flow, assuming that the flow conditions remain static for that long [65]. As a result, even for measurement points where the wind tunnel temperature is held constant for a few minutes, see Fig. 12, the experimental airfoil temperature distribution follows the C_f distribution, rather than a monotonically increasing temperature after transition as expected from computed T_w. Thus if the flow changes within a "short" time, the temperature distribution on the surface will be a function of both the current flow and the historical flow.

The original idea of DIT, as detailed by Raffel et al. [66,67], is to take the difference between two infrared images with a small time separation. The difference will thus include only information related to the changes between those time points, allowing the use of infrared thermography for unsteady flows. Similar to the idea for boundary layer detection by σC_P above, it is assumed that for many subsonic flows that the strongest "feature" seen in a differential flow will be the movement of the boundary layer transition position. As seen in Fig. 13, the differences between two infrared (IR) distributions results in a peak at the boundary layer transition position for the mean condition between the times/angles of the two IR distributions. This can also be used for the analysis of infrared images for fine static polars, and can be useful when the temperature distribution would otherwise be difficult to analyse by hand [8]. As validated against experiment by Richter et al. [58] (Fig. 14) and against computations by Gardner et al. [65], the position of the DIT peak corresponds to the mean 50% intermittency transition position with a small systematic error, see Fig. 15. There are two systematic errors in the DIT measurement: Firstly the selection of images which are too widely separated in time results in an error in the prediction of the mean peak position, and secondly an irreducible thermal hysteresis is created due to the propagation of heat into the body.

The use of DIT for boundary layer transition measurement has been the subject of extensive analysis [8,61,62,65,68]. The requirements for a DIT measurement are quite strict. The surface must have a large IR signal so that the difference between two images will also have a large signal. This generally requires creating a temperature difference between the surface and the flow (as is also commonly used for IRT measurements [69]), which can be created by using a heat-lamp [66] or by using sunlight combined with a rapid change in the operating conditions [70]. There is some disagreement in the literature about the importance of the heating method, with some experimentally observing it to be critical [71], whereas others theoretically noting it to be unimportant [68].

Secondly, the use for unsteady flows on moving objects requires that the image is frozen. This can either be achieved by using short imaging times [68,70] or by using a rotating mirror so that the image of the moving object is slowed, allowing longer exposure times [72]. This second method has been successfully used for a number of wind tunnel experiments [60,73,74], resulting in an increase in the exposure time by a factor of four over flight experiments where the careful alignment of the rotating mirror with the axis of the rotor is not possible [68]. For tests on a hovering rotor, simply using a short exposure time is generally sufficient to generate IR images for non-DIT analysis [70,75]. The optimisation of the separation time between the two DIT images is important, since larger image separations improve the signal-to-noise ratio of the difference image (more changes take place over a longer time), but increase the systematic error in the DIT measurement, see Fig. 15. The optimisation can either be undertaken for an entire measurement [8], or an adaptive image separation based on a minimum required signal to noise ratio can be computed for each instant of the unsteady flow [61].

There are only two works which have used DIT for transition detection for a helicopter in forward flight up to the current time: Overmeyer et al. [74] and Gardner et al. [68]. A helicopter rotor in forward flight experiences a variation in the inflow total temperature during a rotation which distinguishes it from other unsteady flows with constant inflow. This variation in the inflow total temperature means that a separate heating of the rotor is not necessary, since the surface-

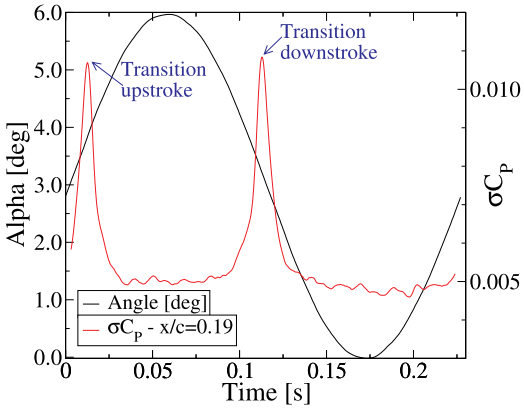

Fig. 11. Pressure signal analysis allowing transition detection on a pitching airfoil, from Ref. [58]. The passage of the laminar-turbulent transition over the sensor is visible as a peak in the standard deviation of pressure.

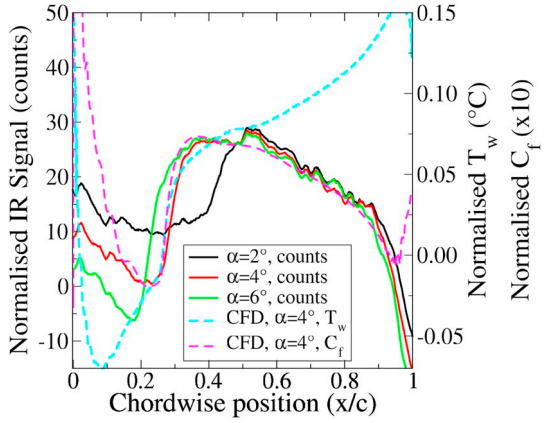

Fig. 12. Unheated DSA-9A airfoil surface temperature, with the computed adiabatic temperature distribution shown for comparison. The computations use a manually fixed boundary layer transition at the experimentally measured transition point, from Ref. [68].

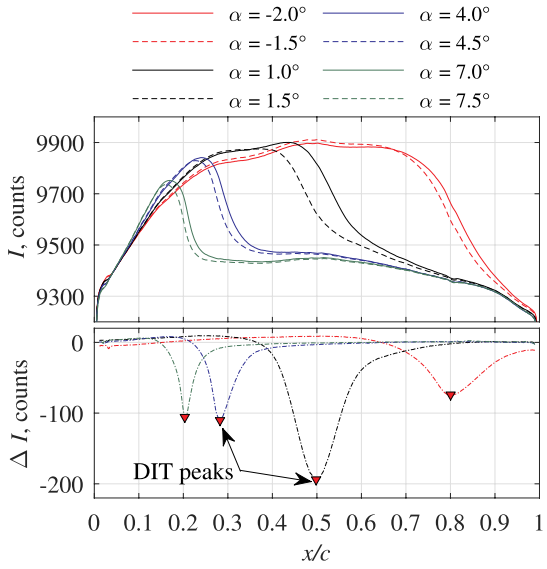

Fig. 13. Difference peaks from subtracted IR signals for static airfoil angles illustrating boundary layer transition detection using DIT, from Ref. [8].

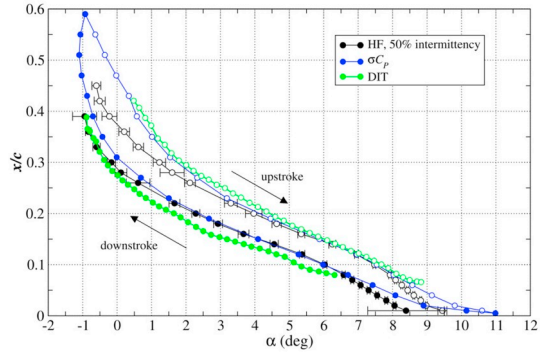

Fig. 14. Validation of DIT against hot-film and σC_P data for a pitching airfoil, from Ref. [58]. The boundary layer transition position measured by DIT has a small time delay compared to the other methods, which is within the experimental accuracy for a pitching frequency of 6.6 Hz.

flow temperature difference is inbuilt in the aerodynamic system (and in fact heating the surface reduces the measured IR signal). However the constant variation in the recovery temperature means that all parts

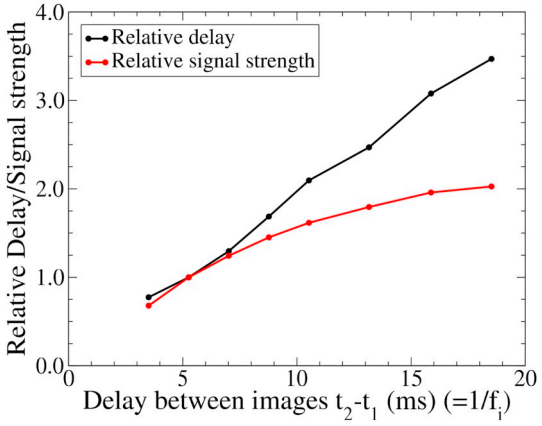

Fig. 15. Validation of DIT showing hysteresis and signal change with image separation, from Ref. [65].

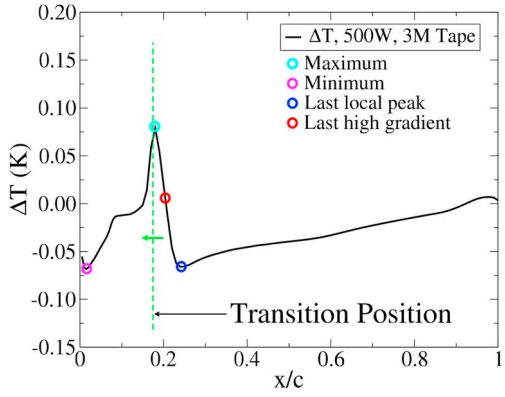

Fig. 16. Alternative methods of selecting the boundary layer transition position from a DIT signal for forward flight, from Ref. [68].

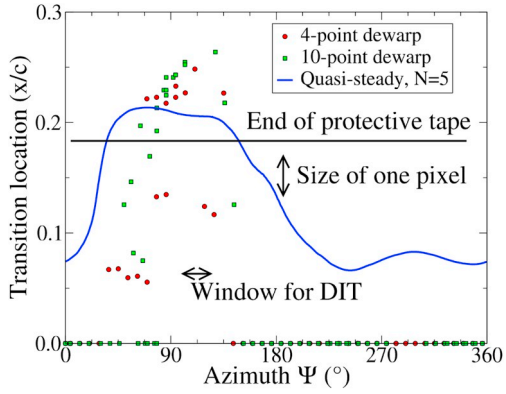

Fig. 17. Proof of principle measurement of boundary layer transition using DIT on a helicopter in forward flight at 80 kts and 1700 ft, from Ref. [68].

of the rotor undergo a constant thermal cycling which is a dominant feature of the DIT images.

The analysis thus requires a different approach than the peak detection used for standard DIT images. In Fig. 16, several options are shown, and the image should be evaluated from the trailing edge rather than from the leading edge. Of the options shown, the "last high gradient" appears to be the most robust over a variety of conditions, but an additional systematic error of up to 5% chord is incurred in the analysis of these images. The analysis of DIT images for a helicopter rotor in forward flight is a topic of ongoing investigation. Fig. 17 shows the results of a measurement of transition using DIT on the main rotor of a

helicopter in forward flight at 80 kts and 1700 ft [68]. The initial results show that the measurement is possible, but the relatively coarse optical resolution and the low signal to noise ratio make the results only sufficient to exclude the worst errors for numerical comparisons. In fact the results in Fig. 17 show that the numerical estimates of the boundary layer transition position appear to be rather good.

In contrast, DIT has allowed high-quality transition maps to be generated for the reference case of a rotor with axial inflow [60], see Fig. 18. This data compares well to σC_P data, and is of sufficient quality to allow calibration of CFD codes, see Fig. 19. This is a considerable improvement over the σC_P data previously available, shown as points on Fig. 19, since the DIT data has a higher resolution both in the chordwise and the spanwise directions. In particular, the CFD can be calibrated to match the transition position as a single radial coordinate rather well [29], but the variation of transition position over the rotor radius must be matched by correctly modelling the flow. It is hoped that the availability of high-quality experimental data for calibration and validation will lead to the next generation of improvements in the modelling of boundary layer transition for unsteady flows.

Local infrared thermography (LIT) is an alternative method of infrared image evaluation, which has been validated against σC_P and DIT data for a pitching airfoil [61]. LIT is currently only practical for highly periodic flows due to the requirement for a very fine discretisation in the time or period axis. This fine discretisation has initially been achieved by carefully timing the medium-speed IR camera at roughly 100 Hz to be slightly offset to the period of the unsteady pitching airfoil, so that after 50 s a highly sampled single phase with 5000 images can be reconstructed. Clearly in the future it would be desirable to have an infrared camera which would operate in the multiple kilohertz range for this technique.

In contrast to DIT, which is a spatial analysis of a pair of infrared images, LIT analyses each single pixel of a large set of IR images in time, see Fig. 20, which is rather analogous to the analysis of a single high-speed thermocouple. For a pixel which is sometimes in laminar and sometimes in turbulent flow, and which is located on a heated surface which is in thermal equilibrium, when seen over a multi-cycle time frame, the surface temperature is constantly changing. When the flow at the pixel is laminar, then the surface heat flux is low, and the surface heating exceeds the heat flux to the flow, resulting in the surface warming. In contrast, when the flow at the pixel is turbulent, then the heat flux to the flow exceeds the surface heating and the surface cools. The interface between the laminar and turbulent flows, the boundary layer transition point, is then seen in the time history of the single pixel as an inflection point between positive and negative temperature gradients.

The primary advantage of the LIT method is that the pixel-wise evaluation method is directly applicable to the 3D analysis of boundary layer transition on a surface, since the analysis does not rely on cut-extraction and analysis as for DIT. The requirements for the measurement are much higher, however, needing at least hundreds, if not thousands of IR images over a periodic cycle.

4.4. Temperature sensitive paint

Similar to pressure sensitive paint, temperature sensitive paint (TSP) uses photokinetic interactions to measure the surface temperature using an applied florescent coating, see Liu and Sullivan [33]. Excitation light at short wavelengths is absorbed by the light-sensitive luminophores, and the dye molecules emit light at longer wavelengths. The amount of florescent emission is reduced by thermal interactions with the surrounding material, the amount of which depends on the local temperature. Higher local temperature reduces the amount of light emitted and the luminescent lifetime decay time. TSP can be used in essentially the same way as IR thermography to measure boundary layer transition [76], with the advantage that high-resolution visible light cameras can be used instead of the low resolution IR sensors.

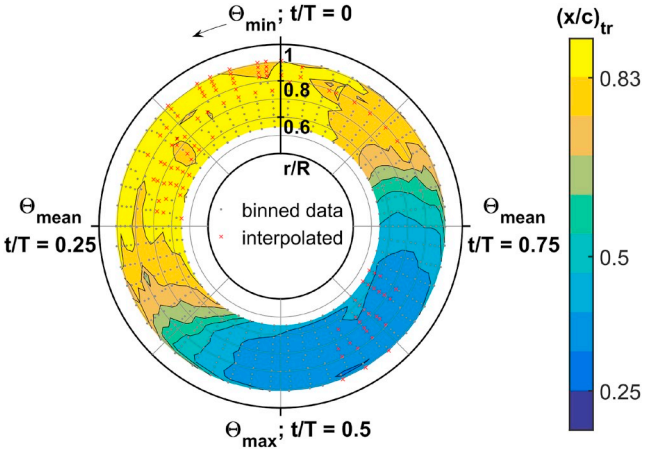

Fig. 18. Transition position map on the RTG pitching axial inflow rotor measured using DIT, from Ref. [60].

The TSP used by the DLR is based on ruthenium phenanthroline [Ru (phen)] inside a polyurethane binder matrix, as described in more detail by Yorita et al. [77]. The data is recorded by the intensity method, and the paint was uncalibrated since only the step in temperature due to the boundary layer transition is necessary. Although a rotating mirror has been used [73], this has been found to be unnecessary for the rotor without cyclic flow [20]. The same short-exposure method is also used for the short-duration Ludwieg tube in Göttingen [78]. The use of temperature sensitive paint for boundary layer transition measurement for helicopters Göttingen has currently been restricted to the hovering rotor case which has rapid movement, but static aerodynamics in the frame of the rotor blade. An extension of TSP to unsteady aerodynamics is possible [79] and an extension to rotor flows using the same image analysis techniques as DIT is planned for the future.

The high-quality static TSP reference data for the RTG rotor, see Fig. 21, has been used for the fine adjustment of the computational parameters before the numerical investigation of unsteady pitching using similar σC_P data to that seen in Fig. 14. The numerical investigation of the RTG axial inflow rotor test stand [28,29], has shown that using a stiff rotor of this type leads to an improved confidence in the aerodynamic numerical methods, since a prescribed trim and stiff structure make the identification of errors unambiguous. At this point the RTG test stand can be well computed using the DLR-TAU, IAG-FLOWer and Onera-elsA URANS codes considering the RTG rotor as an isolated rotor in a farfield boundary.

5. Flow topology measurement

5.1. Stall detection

In addition to the boundary layer transition detection, the pressure sensor analysis can be used to detect stall in a dynamic system [24]. As seen in Fig. 22, the standard deviation for times where the flow is stalled over the pressure sensor is much greater than for either fully attached flow or boundary layer transition. If a similar approach is used for IR images, then the stall can also be detected in a dynamically pitching system. Infrared data can also be used to detect static flow separation [64,80], but the extension to dynamic or transient stall is a recent development. For the infrared data, images which are close in time, but for different pitching cycles are subtracted to get the differences between the images. The standard deviation is then computed for a small spatial area of the difference image, and for attached flow the differences between two images is small, whereas for separated flow the differences between two images is large. As seen in Fig. 23, the comparison between pressure analysis and IR analysis is good, and the stall is detected well in both time and space [7,81]. A further comparison

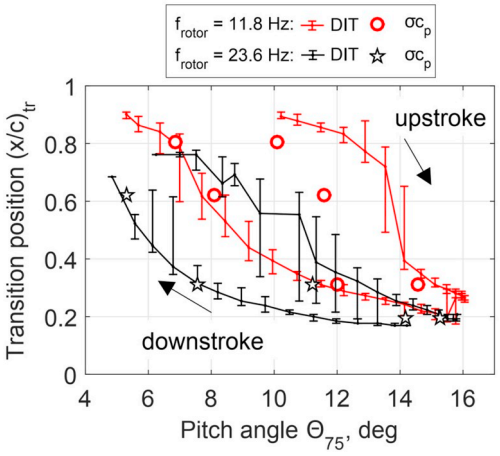

Fig. 19. Comparison of measured boundary layer transition positions between DIT and σC_P data on the RTG rotor, from Ref. [60].

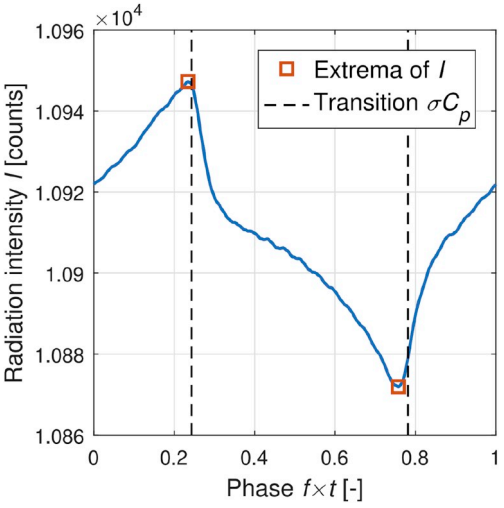

Fig. 20. Analysis of single-pixel data over time for the measurement of dynamic boundary transition movement by local infrared thermography (LIT), from Ref. [61].

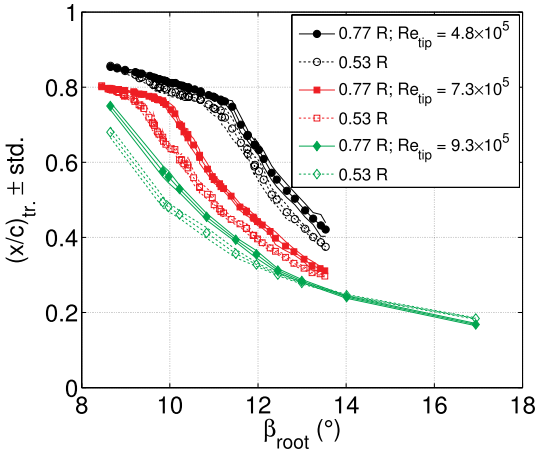

Fig. 21. Example static boundary layer transition positions from TSP data for different positions and rotation rates on the RTG rotor with static root angle, from Ref. [20].

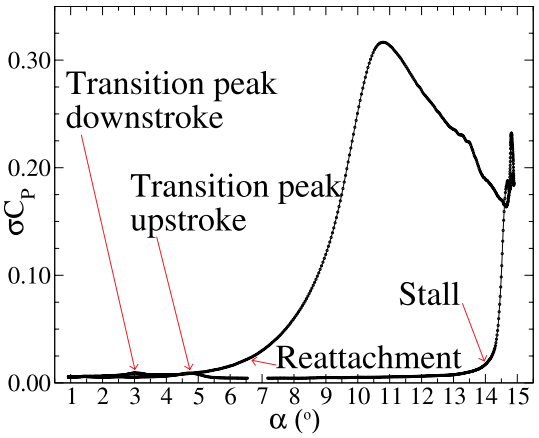

Fig. 22. Pressure signal analysis of the standard deviation allowing stall detection at the sensor position on a pitching airfoil, from Ref. [24].

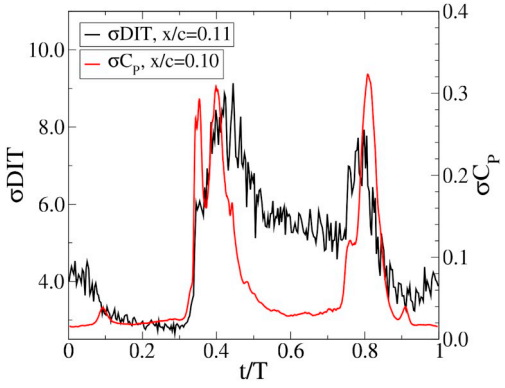

Fig. 23. Comparison of pressure analysis and IR signal analysis for stall detection on a pitching airfoil, from Ref. [7].

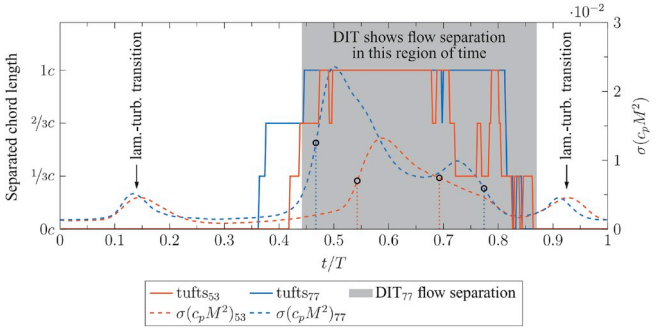

Fig. 24. Comparison of stall detection methods on the pitching RTG rotor with axial inflow, from Ref. [13]. Pressure analysis and DIT give similar results, and the tuft analysis shows a similar stall region, but the flow separation is promoted by the addition of the tufts to the surface.

has been undertaken for a rotor [13], in which additionally the analysis of photographic footage of tufts attached to the suction side of the rotor was compared with pressure and IR data, see Fig. 24. The tuft data shows a systematic error due to the introduction of the tufts into the flow, in this case resulting in earlier stall and later reattachment than without the tufts installed.

5.2. High-speed particle image velocimetry

Particle image velocimetry (PIV) is a method of flow field velocity measurement using small seeding particles which follow the flow. The basic PIV technique is described in Ref. [82] and in Ref. [83]. As most often used for unsteady helicopter flows, PIV uses a laser light sheet to illuminate a thin section through the flow with two pulses which are separated by a small time. Optically sharp particle image pairs are acquired on two cameras, for a total of four images of the flow. The use of a stereoscopic two-camera system accounts for and quantifies the velocity component perpendicular to the light sheet, giving access to the three-component velocity vector in a two-dimensional plane of interest. Normal PIV lasers, consisting of a laser pair, operate with a maximum repetition frequency of approximately 10 Hz. High-speed PIV rapidly repeats the acquisition of image pairs with a frequency of 1000 Hz or more and requires lasers and cameras which offer this functionality.

The department of helicopters in Göttingen uses both high-speed PIV and low-speed PIV, nearly exclusively as a stereo light-sheet setup, see Fig. 1a, for the observation of rotor-blade aerodynamics and rotor wake aerodynamics. Both methods allow a near-perfect “freezing” of the flow, due to the short length of the laser pulses and the small image separation time compared with the flow time constants. Low-speed PIV offers much higher laser power, which allows larger observation fields under difficult measurement conditions, but flow phenomena cannot be tracked, and the data analysis relies more on statistical correlations. High-speed PIV allows direct image-to-image tracking of unsteady flow phenomena and direct analysis of data concerning the tracks can also be extracted. As seeding, Laskin-nozzle aerosolised DEHS with an approximate 1 μm diameter is used. An overview of many contributions to particle image velocimetry in helicopter aerodynamics can be found in Ref. [84].

One of the first experiments to use high-speed PIV on a dynamic stall test case was Mulleners et al. [85,86], who applied stereo PIV to a pitching OA209 airfoil at 50 m/s. The data analysis of the instantaneous images, see Fig. 25, showed that individual subvortices could be identified and tracked. Additionally, the data could be analysed using proper orthogonal decomposition (POD), identifying modes which only appeared during stall, and thus allowing an alternative method of identifying the flow separation time. Additionally, qualitatively different regions of the flow could be identified using Lagrangian coherent structure analysis. Unexpectedly, it could also be shown that the unsteady separated flow generated by a statically inclined airfoil at high angle of attack generated a bistable separation point, whose position and movement could also be reconstructed using high-speed PIV [87]. The advantage of high-speed PIV for the analysis of flow control devices to reduce dynamic stall could also be demonstrated, see Fig. 26. The measurements of Heine et al. [87] and Mulleners et al. [86] also showed the utility of high-speed PIV synchronised with surface pressure measurements to better understand those measurements, also in test cases where PIV was not available.

Later investigations showed that while the analysis of the POD mode time development coefficients was useful, the analysis of the POD mode shapes was only of limited use, and dynamic mode decomposition (DMD) was unsuitable for the analysis of dynamic stall [88]. However the correlations in flows between the sizes of the flow structures and the energy contained in the modes means that reconstruction of a flow excluding higher POD modes can be used effectively as a filter of fine structures, see Fig. 27. This approximation is particularly useful for understanding the method by which a flow control device acts on the flow [89], since the fine structures are usually an indirect byproduct, and the larger structures can be more directly attributed to a particular flow control function.

Particle image velocimetry synchronised with pressure measurements has become a standard method for many groups [90–95]. In particular, low-speed phase-averaged PIV, which has been a standard method for helicopter flow research [23,96] can often give results comparable with high-speed PIV, if only averaged PIV images are required. As seen in Fig. 28, the dynamic stall on a rotor is taken using a low-speed PIV system every third rotor cycle, whereas in Fig. 29 a high-speed system is used. Both are synchronised with the pressure sensor system and allow better understanding of the pressure data. The high-speed PIV data allowed the tracking of single structures, but with an increased experimental effort compared to the low-speed PIV.

In contrast to dynamic stall, a very large number of experiments have been conducted using PIV to examine rotor wakes [97–101]. The characterisation of tip vortices (i.e., their spatial location relative to the blade, core size, peak swirl velocity, vorticity, and circulation) is essential to understanding flow phenomena which appear on rotors including blade-vortex interaction (BVI) and dynamic stall due to blade-vortex interaction, and also for the accurate computation of rotor loads and performance [102–107]. A shift from using laser Doppler velocimetry (LDV) to PIV, see Refs. [108–110] has resulted in lower time-accuracy, but a better understanding of phenomena including vortex aperiodicity for both full-scale [111,112] and small scale rotors [113].

The research group at the DLR in Göttingen has recently followed two approaches to the wake characterisation. Firstly, using the RTG rotor test stand for a rotor with cyclic pitch in axial inflow, see Fig. 30, exact low-speed PIV measurements of the vortex have been made, see Refs. [18,19,114]. These experiments very finely scan the rotor azimuth, but are limited both in spatial resolution and in their ability to investigate the vortex shape, due to the particle void which extends from the core to near the edge of the vortex, see Refs. [115,116]. These experiments are then carefully computed using unsteady CFD with modern turbulence modelling [117,118], which accurately reproduces the blade aerodynamics and the data across the vortex core, but which has difficulties correctly reproducing the time history of the vortex characteristics. By combining these two approaches, a better understanding of the vortex generation and propagation is reached than for each method alone. Similarly, the vortex generated by the unsteady pitching wing has been investigated using high-speed PIV [16] and CFD [17], and a good agreement could be found between CFD and PIV for even for dynamic pitching into stall, see Fig. 31 and it could additionally be shown that an appropriate scaling could be used to match the pitching wing and rotating blade results [117], see Fig. 32.

The second approach has been to perform high-speed PIV on helicopter rotors in the wind tunnel [119,120], on model helicopters in free flight [21], or on full-scale helicopters in free flight [22]. Here the experiments are less well characterised, but measure the far more complex flow situations including maneuvering flight, however the computation of the configurations is currently outside the capabilities of the Göttingen group. Similar efforts by NASA at Langley [121,122]

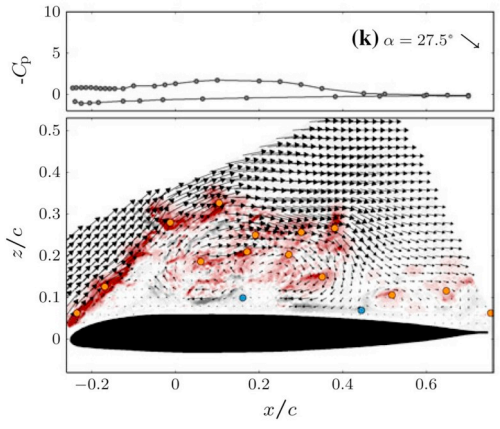

Fig. 25. Dynamic stall vortex, from Ref. [85]. The dynamic stall on a pitching airfoil was measured using high-speed stereo PIV and analysed using Eulerian structure detection. The instantaneous pressure distribution is presented for comparison.

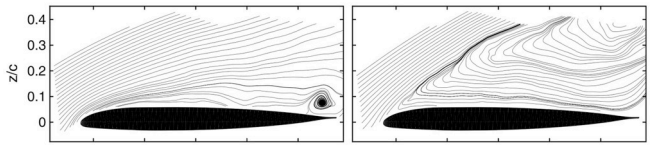

Fig. 26. Flow control comparison Left: with LEVoGs Right: Clean, from Ref. [87]. The dynamic stall on a pitching airfoil was measured using stereo high-speed PIV, and the reduction in the size of the stalled region in the left image indicates the effectiveness of the dynamic stall control vortex generators.

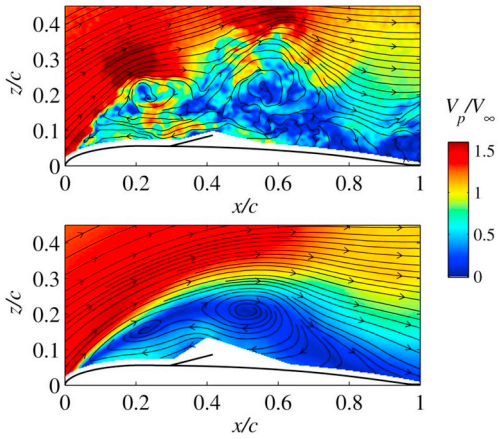

Fig. 27. Use of POD flow filtering on high-speed PIV data taken for a pitching airfoil with dynamic stall controlled by a back-flow flap, from Ref. [89]. Top: Instantaneous unfiltered Bottom: Small structures filtered.

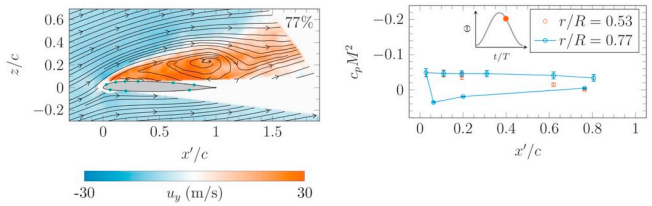

Fig. 28. Low-speed stereo PIV of dynamic stall at r/R = 0.77 on the RTG pitching rotor with axial inflow, from Ref. [13]. The separated flow is accelerated tipward while the attached flow is moving rootward. The instantaneous PIV image was analysed to find the boundary layer separation point and correlated with the instantaneous pressure distribution.

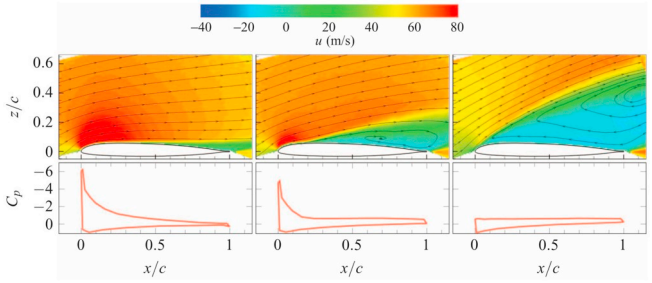

Fig. 29. Monitoring of dynamic stall using high-speed stereo PIV on a pitching finite wing, correlated with instantaneous pressure measurements at three spanwise stations, from Ref. [11].

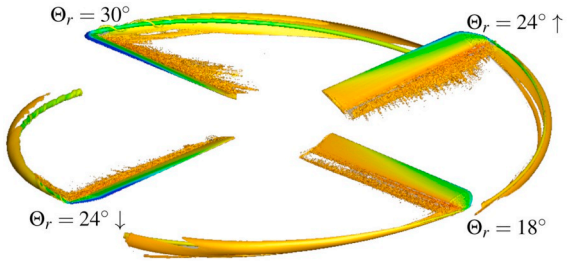

Fig. 30. CFD image illustration the change in the blade tip vortices over one cycle of the RTG rotor pitching with axial inflow, from Ref. [118].

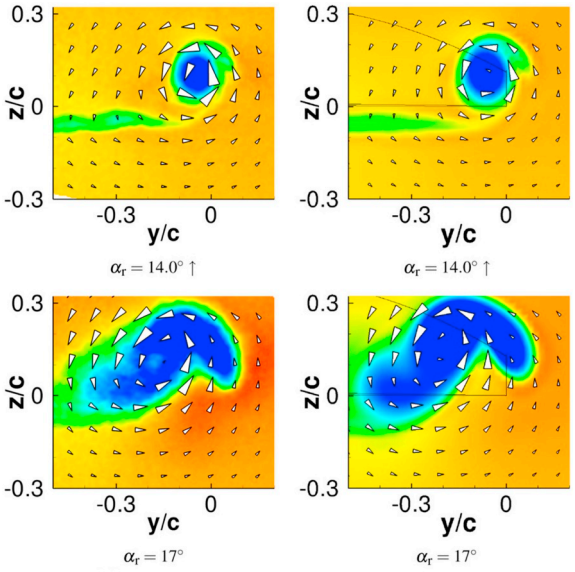

Fig. 31. Comparison of pitching wing tip vortices (Left) PIV, (Right) CFD, from Ref. [17]. The top images shows the blade tip vortex and blade wake for attached flow and the bottom images show the blade tip vortex for the blade in dynamic stall.

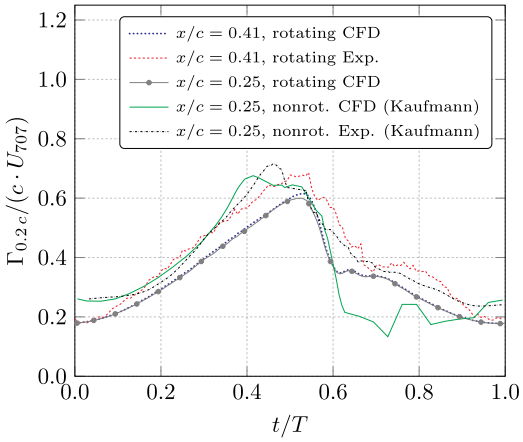

Fig. 32. Comparison between finite wing and pitching rotor vortex circulations, from Ref. [118]. The analysis shows a direct comparability between the two test cases.

have also shown a good comparison to CFD computations using Helios [123].

The model helicopter experiments have the advantage that they can be conducted indoors, so that laser safety and wind can be controlled, and the PIV view field is relatively large compared to the helicopter, see Fig. 33. Additionally, model helicopters have a very large power to weight ratios, which that the effects of maneuvers (primarily strengthening the wake) can be easily separated from the effects compared to static hover or constant flight. In Fig. 33, the whole vortex system at the front of the rotor can be seen, including the start of vortex paring between the last two vortices. In contrast, high-speed PIV on the vortices of a helicopter in flight is strongly limited by the available size

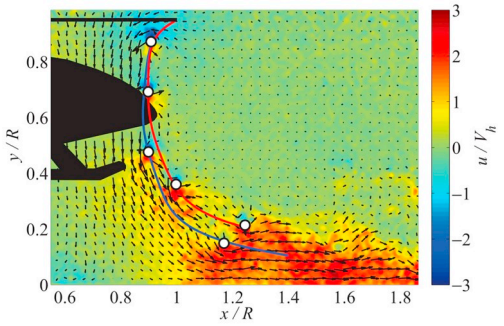

Fig. 33. Tip vortices of a model helicopter in maneuvering flight, from Ref. [21]. The flow field is measured using stereo PIV and the vortex cores are marked with white dots.

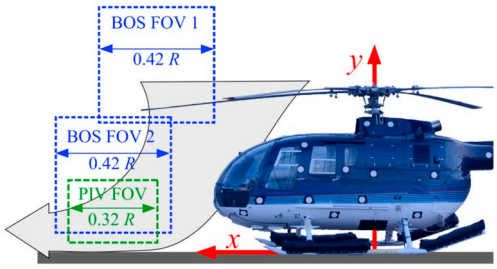

Fig. 34. Relative fields of view for PIV and BOS systems for a flight test to investigate tip vortices in maneuvering flight, from Ref. [22].

of the PIV window, which is now much smaller than the helicopter, see Fig. 34, due to limitations in laser power and camera resolution. In this case the larger fields of view of background oriented schlieren (BOS) can be used to further understand the flow field, which will be discussed more in the next section. Additionally, the experiments are subject to variations in wind, and laser safety (including laser goggles for the helicopter pilots) which add to the experimental difficulty.

An essential part of blade vortex measurement is the knowledge of the blade position. For elastic rotor blades, the trailing edge position can vary considerably from its nominal position, and thus vortex trajectories should be related to the true rotor tip trailing edge position [116]. This measurement can be performed optically using stereo pattern recognition (SPR) (also known as multi-camera photogrammetry), which has often been performed on rotors, [124]. Wolf et al. [125] suggest that the achievable accuracy of SPR measurements on a full-size rotor is around ±0.1° in torsion, and ±1 mm in position. For the unsteady measurement of the rotor tip position in Göttingen a simplified optical tracking system with a single camera is used to follow two dots painted on the rotor tip [13]. This approach has significantly reduced effort for the setup and calibration, and most importantly the evaluation is significantly simpler. The single camera is mounted to observe along the blade axis toward the hub at a single azimuthal position and triggered when the blade is in position, once per cycle and has an accuracy of around ±0.1° in torsion, and ±1 mm in flap. This approach has also been used for aircraft in flight [126].

In the future, it appears that high-speed volumetric particle image measurements will have a crucial advantage over planar PIV, of resolving complex 3D wake shapes. Although planar PIV data can be reconstructed to pseudo-volumetric data [116], the recent development of the “Shake-the-Box” (STB) method [127] allows volumetric measurements with high particle densities and direct measurement of the particle acceleration, using a Lagrangian particle tracking algorithm which is optimal for vortex measurement. This can be used to resolve the complex shape of turbulence, but also the interaction between primary and secondary structures in a rotor wake [128]. Fig. 35 shows the analysis of secondary vortex structures in the wake of a hovering rotor, which appear to be responsible for vortex breakdown in this type of flow. The colouring differentiates between the primary vortices (grey), and the positive (red) and negative (blue) secondary vortices.

5.3. Background oriented schlieren for vortex detection

Background oriented schlieren (BOS) is a method of detecting density gradients integrated over the line of sight through a flow, using a camera focused on a high-contrast structured background with low autocorrelation values. The basics of BOS, as well as an overview of its development and use can be found in Refs. [129,130]. The normal evaluation of BOS relies on a reference image which is cross-correlated with the measurement image to give displacements which are related to the density gradient. The particular advantage of BOS is the ability to visualise density-changing flow structures (like vortices or shear layers) using much larger fields of view than would be possible for PIV, see the comparison in Fig. 34. Additionally, the reduced lighting and focus constraints compared to PIV mean that high-speed visible light cameras can be used to acquire videos of the flow-phenomena, for example as [22]. A variety of backgrounds can be used for BOS, however experiments show that using retroreflective synthetic dot-patterns provides the highest quality results [131]. For helicopters in flight, this is not always possible, and here natural backgrounds [132] (grass, leaves, gravel, etc.) can offer an alternative which also performs acceptably for some variants [133]. An alternative is to use speckle-BOS [134], which uses laser-speckles as the structured background. This method potentially allows the camera focus to move to the image plane instead of the background, but a direct comparison by our group found an increased noise-induced pixel shift for our lasers [135].

For in-flight measurements, generally a reference-free BOS is used, which uses two subsequent images in a high-speed video for the BOS analysis, resulting in a double-image of the object to be compared. Fig. 36, left shows a helicopter in front of a synthetic background in hover. In this case the use of standard reference BOS would theoretically have been possible, but the sunlight used to illuminate the background was changing too rapidly to be able to use the reference image. In Fig. 36, right, a flare maneuver was performed against a natural background, and the utility of the BOS measurement for flight tests can be seen. Additionally differential BOS can be used to image the rotor blades of a helicopter in-flight [132], which allows the analysis of vortices under free-flight with strong maneuvers [126].

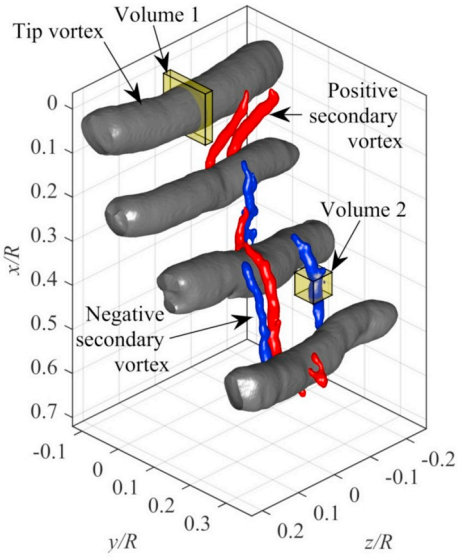

Fig. 35. Tip vortex and secondary vortex system of a model helicopter in hover, from Ref. [128]. The flow field is measured using the volumetric Lagrangian particle tracking method STB for time-resolved flowfields.

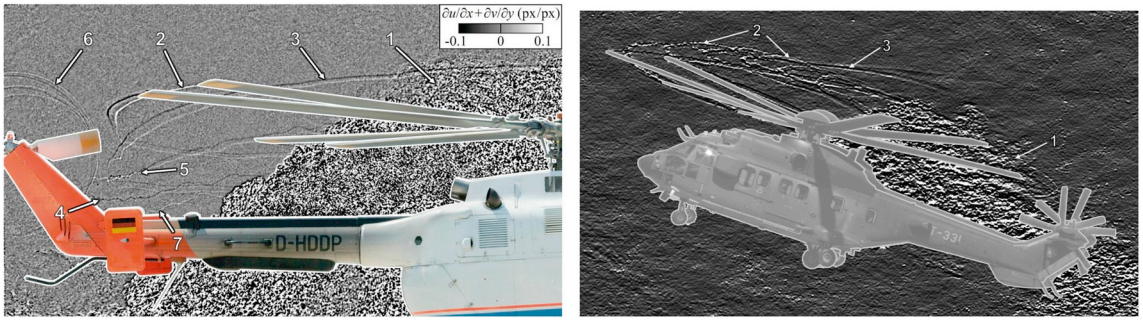

Fig. 36. Reference-free in-flight BOS to visualise the rotor tip vortices and wake (Left) Retroreflective synthetic dot background, from Ref. [131] (Right) natural stone background, from Ref. [133].

Fig. 37 illustrates a direct comparison between high-speed BOS and PIV. In this case, the fields of view are as Fig. 34, and in Fig. 37, left the helicopter vortex system between the rotor and the ground is captured. This is a similar setup to that used in small scale by In Fig. 37, right both the PIV and BOS fields contain the same vortices, which can be directly compared. The sequence shows vortex pairing in the downwash of a helicopter in slow maneuvering flight near to the ground, and the BOS data is integrated over the line of sight, meaning that the vortex positions are less clear than for the PIV data. This problem can only be solved by using multiple cameras, since the vortex will give the strongest schlieren signal when it is aligned with the camera, rather than when it is in the desired position. A tracking of the vortex positions in 2D can be useful, see Ref. [18], but requires good camera positioning. In this case, a reconstruction of the vortex density assuming axisymmetry is possible, so long as the resolution of the BOS data is high enough [136,137].

Although the 3D reconstruction of the vortex density distribution is theoretically possible, this has not yet been successfully undertaken. However the helicopter vortex system geometry can be reconstructed in 3D space [138]. An epipolar method for vortex reconstruction [139] must be used, since the vortices are an undefined line. The full reconstruction using multiple cameras has been demonstrated by Bauknecht et al. [140] for a hovering helicopter in a quarry. Fig. 38 shows the reconstruction of a vortex system using multiple-camera BOS, and a comparison to computation. The 3D reconstruction has gaps where the helicopter geometry interrupts the view of the 2D projections, or where the quality of the natural stone background is too poor for the BOS cross-correlation, so that the reconstruction is not complete. The

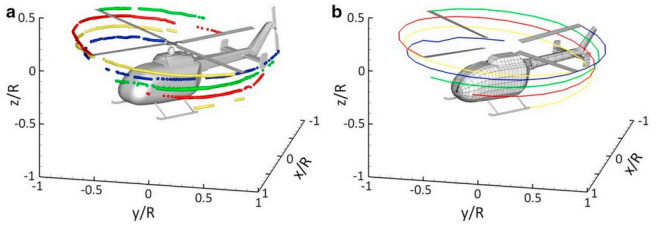

Fig. 38. Helicopter vortex system Left: Measurement with reconstructed vortex system geometry from multicamera BOS measurements, Right: Computation with panel method, from Ref. [140].

reconstruction has not yet been undertaken as an unsteady process, although the method is not theoretically different than the single reconstruction.

6. Summary and conclusions

This article has summarised the work of the helicopter aerodynamics group in Göttingen on measurement techniques for unsteady helicopter rotor flows. Besides the relatively standard pressure and heat flux measurements, four new techniques for the detection of dynamically moving boundary layer transition have been developed and validated: Pressure sensor analysis, differential infrared thermography, local infrared thermography and the automated analysis of hot-film data for dynamic boundary layer transition movement. Similarly, the new techniques of pressure sensor analysis and differential infrared thermography have been validated against tuft measurements for the

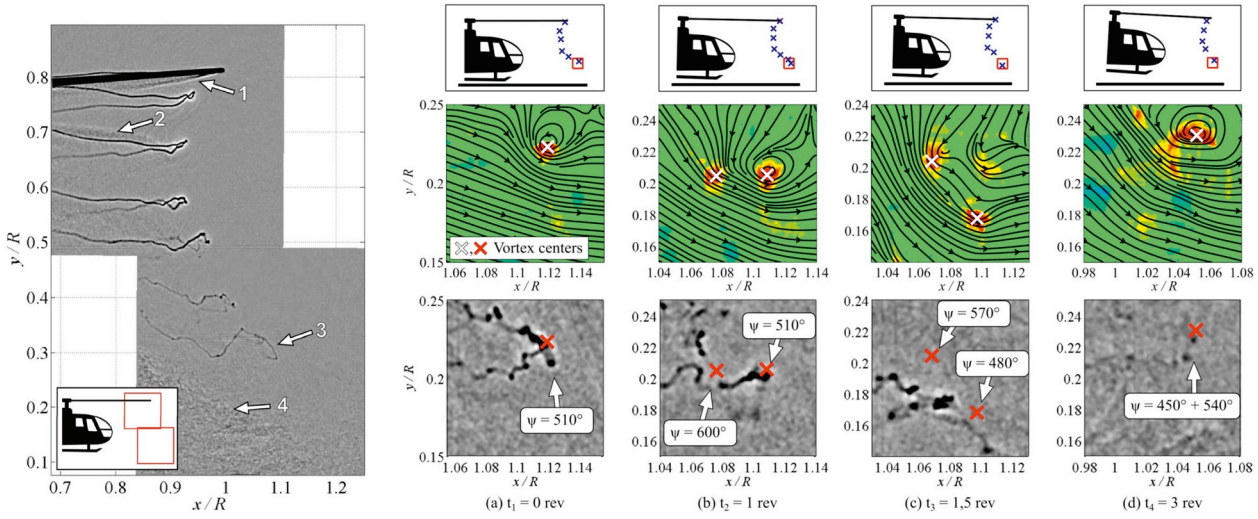

Fig. 37. Left: Helicopter vortex system with BOS, Right: Tip vortex pairing of a BO105 helicopter in maneuvering flight comparing a time-series of PIV and BOS data taken simultaneously of the same region, from Ref. [22].

detection of dynamic stall and other transient flow separation events.

Particle image velocimetry and background oriented schlieren have been used for the analysis of the unsteady off-body flow, and synchronised PIV-BOS-pressure measurements have allowed direct comparisons between different methods. The Lagrangian volumetric PIV variant, shake-the-box, has been used to analyse secondary vortex structures in the vortex wake.

A combination and comparison of the experimental work with numerical analyses has shown that the data from both methods can be used to better understand the flow phenomena present on unsteady flows of the type present on helicopter rotors.

Acknowledgments

This review article is based on the cited work of many scientists. We are very much indebted to those researchers in our group, at the DLR and worldwide. Additionally, the work of the DLR technicians, DLR workshops and DNW wind tunnels is gratefully acknowledged. This review article was financed by the DLR basic financing.

References

[1] H. Mai, G. Dietz, W. Geissler, K. Richter, J. Bosbach, H. Richard, K. de Groot, Dynamic stall control by leading edge vortex generators, J. Am. Helicopter Soc. 53 (1) (2008) 26–36, https://doi.org/10.4050/JAHS.53.26.

[2] A.D. Gardner, K. Richter, H. Mai, A.R.M. Altmikus, A. Klein, C.-H. Rohardt, Experimental investigation of dynamic stall performance for the EDI-M109 and EDI-M112 airfoils, J. Am. Helicopter Soc. 58 (1) (2013), https://doi.org/10.4050/JAHS.58.012005.

[3] B. Heine, K. Mulleners, A. Gardner, H. Mai, On the effects of leading edge vortex generators on an OA209 airfoil, 10th ONERA-DLR Aerospace Symposium, Berlin, Germany, 6-8 Oct. 2009.

[4] K. Richter, A. Le Pape, T. Knopp, M. Costes, V. Gleize, A.D. Gardner, Improved two-dimensional dynamic stall prediction with structured and hybrid numerical methods, J. Am. Helicopter Soc. 56 (4) (2011), https://doi.org/10.4050/JAHS.56.042007.

[5] A.D. Gardner, K. Richter, H. Mai, D. Neuhaus, Experimental investigation of air jets to control shock-induced dynamic stall, J. Am. Helicopter Soc. 59 (2) (2014), https://doi.org/10.4050/JAHS.59.022003.

[6] A.D. Gardner, S. Opitz, C.C. Wolf, C.B. Merz, Reduction of dynamic stall using a back-flow flap, CEAS Aeronaut. J. 8 (2) (2017), https://doi.org/10.1007/s13272-017-0237-4.

[7] A.D. Gardner, C.C. Wolf, M. Raffel, A new method of dynamic and static stall detection using infrared thermography, Exp. Fluid 57 (9) (2016), https://doi.org/10.1007/s00348-016-2235-4.

[8] C.C. Wolf, C. Mertens, A.D. Gardner, C. Dollinger, A. Fischer, Optimization of differential infrared thermography for unsteady boundary layer transition measurement, Exp. Fluid 60 (1) (2019), https://doi.org/10.1007/s00348-018-2667-0.

[9] A.D. Gardner, K. Richter, Effect of the model-sidewall connection for a static airfoil experiment, J. Aircr. 50 (2) (2013) 677–680, https://doi.org/10.2514/1.C03201.

[10] A.D. Gardner, C. Klein, W.E. Sachs, U. Henne, H. Mai, K. Richter, Investigation of three-dimensional dynamic stall on an airfoil using fast response pressure sensitive paint, Exp. Fluid 55 (9) (2014), https://doi.org/10.1007/s00348-014-1807-4.

[11] C.B. Merz, C.C. Wolf, K. Richter, K. Kaufmann, A. Mielke, M. Raffel, Spanwise differences in static and dynamic stall on a pitching rotor blade tip model, J. Am. Helicopter Soc. 62 (1) (2017), https://doi.org/10.4050/JAHS.62.012002.

[12] C.B. Merz, Der dreidimensionale dynamische Strömungsabriss an einer schwingenden Rotorblattspitze engl: 3D dynamic stall on a pitching finite wing, Doctoral thesis Leibniz University Hannover, 2016.

[13] T. Schwermer, A.D. Gardner, M. Raffel, A novel experiment to understand the dynamic stall phenomenon in rotor axial flight, J. Am. Helicopter Soc. 64 (1) (2019), https://doi.org/10.4050/JAHS.64.012004.

[14] A.D. Gardner, C.B. Merz, C.C. Wolf, Effect of sweep on a pitching finite wing, J. Am. Helicopter Soc. 64 (3) (2019), https://doi.org/10.4050/JAHS.64.032007.

[15] K. Kaufmann, C.B. Merz, A.D. Gardner, Dynamic stall simulations on a pitching finite wing, J. Aircr. 54 (4) (2017) 1303–1316, https://doi.org/10.2514/1.C034020.

[16] C.C. Wolf, C.B. Merz, K. Richter, M. Raffel, Tip-vortex dynamics of a pitching rotor blade tip model, AIAA J. 54 (10) (2016) 2947–2960, https://doi.org/10.2514/1.J054656.

[17] K. Kaufmann, C.C. Wolf, C.B. Merz, A.D. Gardner, Numerical investigation of blade-tip-vortex dynamics, CEAS Aeronaut. J. 9 (1) (2018) 373–386, https://doi.org/10.1007/s13272-018-0287-2.

[18] J.N. Braukmann, C.C. Wolf, A. Goerttler, M. Raffel, Blade Tip Vortex Characterization of a Rotor under Cyclic Pitch Conditions Using BOS and PIV, AIAA Science and Technology Forum and Exposition, San Diego (CA), USA, 7-11 January 2019.

[19] C.C. Wolf, J.N. Braukmann, W. Stauber, T. Schwermer, M. Raffel, The tip vortex system of a four-bladed rotor in dynamic stall conditions, J. Am. Helicopter Soc. 64 (2) (2019), https://doi.org/10.4050/JAHS.64.022005.

[20] A. Weiss, A.D. Gardner, C. Klein, Boundary-layer transition measurements on Mach-scaled helicopter rotor blades in climb, CEAS Aeronaut. J. 8 (4) (2017), https://doi.org/10.1007/s13272-017-0263-2.

[21] C. Schwarz, A. Bauknecht, S. Mailänder, M. Raffel, Wake characterization of a free-flying model helicopter in ground effect, J. Am. Helicopter Soc. 64 (1) (2019), https://doi.org/10.4050/JAHS.64.012010.

[22] C. Schwarz, A. Bauknecht, C.C. Wolf, A. Coyle, M. Raffel, A full-scale rotor-wake investigation of a free-flying helicopter in ground effect using BOS and PIV, Vertical Flight Society 75th Forum, Philadelphia, Pennsylvania, May 13-16, 2019.

[23] K. Mulleners, K. Kindler, M. Raffel, Dynamic stall on a fully equipped helicopter model, Aero. Sci. Technol. 19 (1) (2012) 72–76, https://doi.org/10.1016/j.ast.2011.03.013.

[24] A.D. Gardner, K. Richter, Boundary layer transition determination for periodic and static flows using phase-averaged pressure data, Exp. Fluid 56 (6) (2015), https://doi.org/10.1007/s00348-015-1992-9.

[25] A.D. Gardner, K. Richter, H. Mai, D. Neuhaus, Experimental investigation of air jets for the control of compressible dynamic stall, J. Am. Helicopter Soc. 58 (4) (2013), https://doi.org/10.4050/JAHS.58.042001.

[26] A.D. Gardner, User Guide for Cp2cl Plusm v3.X: A Program to Provide Forces and Moments from Airfoil Pressure Distributions, DLR-IB, 2014 224-2014 A101.

[27] A.D. Gardner, Investigations of Dynamic Stall and Dynamic Stall Control on Helicopter Airfoils, Habilitation Thesis, University of Clausthal, Institute of Technical Mechanics, 2016 DLR-FB-2016-55.

[28] J. Letzgus, A.D. Gardner, T. Schwermer, M. Keßler, E. Krämer, Numerical investigations of dynamic stall on a rotor with cyclic pitch control, J. Am. Helicopter Soc. 64 (1) (2019), https://doi.org/10.4050/JAHS.64.012007.

[29] K. Kaufmann, P. Ströer, F. Richez, C. Lienard, P. Gardarein, N. Krimmelbein, A.D. Gardner, Validation of boundary-layer-transition computations for a rotor with axial inflow, Vertical Flight Society 75th Forum, Philadelphia, Pennsylvania, May 13-16, 2019.

[30] K. Kaufmann, M. Costes, F. Richez, A.D. Gardner, A. Le Pape, Numerical investigation of three-dimensional static and dynamic stall on a finite wing, J. Am. Helicopter Soc. 60 (3) (2015), https://doi.org/10.4050/JAHS.60.032004.

[31] M. Ramasamy, J.S. Wilson, W.J. McCroskey, P.B. Martin, Characterizing cycle-to-cycle variations in dynamic stall measurements, J. Am. Helicopter Soc. 63 (2) (2018), https://doi.org/10.4050/JAHS.63.022002.

[32] J.H. Bell, E.T. Schairer, L.A. Hand, R.D. Mehta, Surface pressure measurements using luminescent coatings, Annu. Rev. Fluid Mech. 33 (1) (2001) 155–206, https://doi.org/10.1146/annurev.fluid.33.1.155.

[33] T. Liu, J.P. Sullivan, Pressure and Temperature Sensitive Paints, Springer–Verlag, Berlin, 2005, https://doi.org/10.1007/b137841.

[34] A. Weiss, R. Geisler, T. Schwermer, D. Yorita, U. Henne, C. Klein, M. Raffel, Single-shot pressure-sensitive paint lifetime measurements on fast rotating blades using an optimized double-shutter technique, Exp. Fluid 58 (9) (2017), https://doi.org/10.1007/s00348-017-2400-4.

[35] O.D. Wong, N.A. Watkins, K.Z. Goodman, J. Crafton, A. Forlines, L. Goss, J.W. Gregory, T.J. Juliano, Blade Tip Pressure Measurements Using Pressure Sensitive Paint, American Helicopter Society 68th Forum, Fort Worth, Texas, May 1-3 2012.

[36] T.J. Juliano, K.J. Disotell, J.W. Gregory, J.W. Crafton, S. Fonov, Motion-deblurred, fast-response pressure-sensitive paint on a rotor in forward flight, Meas. Sci. Technol. 23 (4) (2012), https://doi.org/10.1088/0957-0233/23/4/045303.

[37] J.W. Gregory, H. Sakaue, T. Liu, J.P. Sullivan, Fast pressure-sensitive paint for flow and acoustic diagnostics, Annu. Rev. Fluid Mech. 46 (2014) 303–330, https://doi.org/10.1146/annurev-fluid-010313-141304.

[38] C. Klein, W.E. Sachs, U. Henne, J. Borbye, Determination of transfer function of pressure-sensitive paint, 48th AIAA Aerospace Sciences Meeting and Exhibit, Orlando, Florida, 4-7 January 2010, https://doi.org/10.2514/6.2010-309.

[39] S. Wiggen, U. Henne, C. Klein, J. Nuhn, W. Sachs, Unsteady surface pressures measured at a pitching Lambda wing with vortex dominated flow and transonic effects, CEAS Aeronaut. J. 9 (3) (2018) 417–427, https://doi.org/10.1007/s13272-018-0293-4.

[40] S. Wiggen, H. Mai, J. Nuhn, T. Büte, C. Klein, U. Henne, W. Sachs, R. Konrath, B. Wrede, Motion induced unsteady aerodynamic loads with development of vortical flow, J. Aircr. 55 (1) (2017), https://doi.org/10.2514/1.C034308.

[41] T. Bencic, Rotating pressure measurements on a scale model high-by-pass ratio fan using PSP at NASA LeRC, 5th Pressure Sensitive Paint Workshop, AEDC, Tullahoma, Tennessee, 1997.

[42] J.W. Gregory, Porous pressure-sensitive paint for measurement of unsteady pressures in turbomachinery, 42nd AIAA Aerospace Sciences Meeting and Exhibit, Reno, NV, 5-8 January, 2004, https://doi.org/10.2514/6.2004-294.

[43] A. Suryanarayanan, B. Ozturk, M.T. Schobeiri, J.C. Han, Film-cooling effectiveness on a rotating turbine platform using pressure sensitive paint technique, J. Turbomach. 132 (4) (2010) 1010–1013, https://doi.org/10.1115/1.3142860.

[44] C. Klein, U. Henne, W. Sachs, S. Hock, N. Falk, U. Beifuss, V. Ondrus, S. Schaber, Pressure measurement on rotating propeller blades by means of the pressure-sensitive paint lifetime method, 51st AIAA Aerospace Sciences Meeting, Grapevine, TX, 2013, https://doi.org/10.2514/6.2013-483.

[45] O.D. Wong, A.N. Watkins, J.L. Ingram, Pressure sensitive paint measurements on 15% scale rotor blades in hover, 35th AIAA Fluid Dynamics Conference and Exhibit, Toronto, 6-9 June, 2005, https://doi.org/10.2514/6.2005-5008.

[46] O.D. Wong, K.W. Noonan, A.N. Watkins, L.N. Jenkins, C.S. Yao, Non-intrusive measurements of a four-bladed rotor in hover-a first look, AHS Aeromechanics Specialists' Conference, San Francisco, CA, 20-22 January, 2010.

[47] T.J. Juliano, D. Peng, C. Jensen, J.W. Gregory, T. Liu, J. Montefort, S. Palluconi,

J. Crafton, S. Fonov, PSP measurements on an oscillating NACA 0012 airfoil in compressible flow, 41st AIAA Fluid Dynamics Conference and Exhibit, Honolulu, Hawaii, 27-30, June 2011, https://doi.org/10.2514/6.2011-3728.
[48] K.J. Disotell, D. Peng, T.J. Juliano, J.W. Gregory, J.W. Crafton, N.M. Komerath, Single-shot temperature- and pressure-sensitive paint measurements on an unsteady helicopter blade, Exp. Fluid 55 (2) (2014), https://doi.org/10.1007/s00348-014-1671-2.
[49] A.N. Watkins, B.D. Leigthy, W.E. Lipford, K.Z. Goodman, J. Crafton, J.W. Gregory, Measuring surface pressures on rotor blades using pressure-sensitive paint, AIAA J. 54 (1) (2016) 206–215, https://doi.org/10.2514/1.J054191.
[50] P. Lorber, F. Carta, Unsteady transition measurements on a pitching three-dimensional wing, 5th Symposium on Numerical and Physical Aspects of Aerodynamic Flows, (Long Beach, CA), January 13-15, 1992.
[51] P.F. Lorber, F.O. Carta, A.F. Covino Jr., An Oscillating Three-Dimensional Wing Experiment: Compressibility, Sweep, Rate, Waveform, and Geometry Effects on Unsteady Separation and Dynamic Stall vol. 30, (November 30, 1992) UTRO Report R92-958325-6.
[52] M. Raffel, F. de Gregorio, W. Sheng, G. Gibertini, A. Seraudie, K. de Groot, B.G. van der Wall, Generation of an advanced helicopter experimental database: the wind tunnel test of the EU project GOAHEAD, 35th European Rotorcraft Forum, Hamburg, 22-25 Sept. 2009.
[53] K. Richter, S. Koch, A.D. Gardner, H. Mai, A. Klein, C.-H. Rohardt, Experimental investigation of unsteady transition on a pitching rotor blade airfoil, J. Am. Helicopter Soc. 59 (1) (2014), https://doi.org/10.4050/JAHS.59.012001.
[54] K. Richter, S. Koch, A. Goerttler, B. Lütke, C.C. Wolf, A. Benkel, Unsteady boundary layer transition on the DSA-9a rotor blade airfoil, 41st European Rotorcraft Forum, Munich, Germany, 1-4 Sept. 2015.
[55] A.D. Gardner, Extraction of Transition Data for the Pressure Sensors for the GOAHEAD Test Case 3-4 vol. 9, DLR-Onera internal memo, June 2018.
[56] C.C. Heister, A method for approximate prediction of laminar-turbulent transition on helicopter rotors, J. Am. Helicopter Soc. 63 (3) (2018) 1–14, https://doi.org/10.4050/JAHS.63.032008.
[57] A. Goerttler, A.D. Gardner, K. Richter, "Unsteady boundary layer transition detection by automated analysis of hot film data", New Results in Numerical and Experimental Fluid Mechanics XI, Notes Numer. Fluid Mech. Multidiscip. Des. 136 (2017) 387–396, https://doi.org/10.1007/978-3-319-64519-3_35.
[58] K. Richter, C.C. Wolf, A.D. Gardner, C.B. Merz, Detection of unsteady boundary layer transition using three experimental methods, 54th AIAA Aerospace Sciences Meeting, San Diego (CA), USA, 4-8 January 2016, https://doi.org/10.2514/6.2016-1072.
[59] A.V. Popov, R.M. Botez, Transition point detection from the surface pressure distribution for controller design, J. Aircr. 45 (1) (2008) 23–28, https://doi.org/10.2514/1.31488.
[60] A. Weiss, J. Braukmann, K. Kaufmann, Experimental and numerical investigations of unsteady boundary-layer transition on a dynamically pitching subscale helicopter rotor blade, 19th ONERA-DLR Aerospace Symposium, Meudon, France June 3-5, 2019.
[61] C. Mertens, C.C. Wolf, A.D. Gardner, Unsteady boundary layer transition detection with local infrared thermography, Darmstadt, STAB (2018) 6–7 November, 2018.
[62] C. Mertens, Unsteady Boundary Layer Transition Measurements with Infrared Thermography: Development of Improved Measurement Schemes, Master of Science Delft University of Technology, 2018.
[63] G.M. Carlomagno, G. Cardone, Infrared thermography for convective heat transfer measurements, Exp. Fluid 49 (6) (2010) 1187–1218, https://doi.org/10.1007/s00348-010-0912-2.
[64] E. Gartenberg, A.S. Roberts Jr., Twenty-five years of aerodynamic research with infrared imaging, J. Aircr. 29 (2) (1992) 161–171, https://doi.org/10.2514/3.46140.
[65] A.D. Gardner, C. Eder, C.C. Wolf, M. Raffel, Analysis of differential infrared thermography for boundary layer transition detection, Exp. Fluid 58 (9) (2017), https://doi.org/10.1007/s00348-017-2405-z.
[66] M. Raffel, C.B. Merz, Differential infrared thermography for unsteady boundary-layer transition measurements, AIAA J. 52 (9) (2014) 2090–2093, https://doi.org/10.2514/1.J053235.
[67] M. Raffel, C.B. Merz, T. Schwermer, K. Richter, Differential infrared thermography for boundary layer transition detection on pitching rotor blade models, Exp. Fluid 56 (2) (2015), https://doi.org/10.1007/s00348-015-1905-y.
[68] A.D. Gardner, C.C. Wolf, J.T. Heineck, M. Barnett, M. Raffel, Helicopter rotor boundary layer transition measurement in forward flight using an infrared camera, Vertical Flight Society 75th Forum, Philadelphia, Pennsylvania, May 13-16, 2019.
[69] A. Quast, Detection of transition by infrared image technique, 12th International Congress on Instrumentation in Aerospace Simulation Facilities (ICIASF 87), Williamsburg, VA, 22-25, June 1987, pp. 125–2134.
[70] K. Richter, S. Schülein, Boundary-layer transition measurements on hovering helicopter rotors by infrared thermography, Exp. Fluid 55 (7) (2014), https://doi.org/10.1007/s00348-014-1755-z.
[71] B. Simon, A. Filius, C. Tropea, S. Grundmann, IR thermography for dynamic detection of laminar-turbulent transition, Exp. Fluid 57 (5) (2016), https://doi.org/10.1007/s00348-016-2178-9.
[72] M. Raffel, J.T. Heineck, Mirror-based image derotation for aerodynamic rotor measurements, AIAA J. 52 (6) (2014), https://doi.org/10.2514/1.J052836.
[73] W. Lang, A.D. Gardner, S. Mariappan, C. Klein, M. Raffel, Boundary-layer transition on a rotor blade measured by temperature-sensitive paint, thermal imaging and image derotation, Exp. Fluid 56 (6) (2015), https://doi.org/10.1007/s00348-015-1988-5.
[74] A. Overmeyer, J.T. Heineck, C.C. Wolf, Unsteady boundary layer transition measurements on a rotor in forward flight, American Helicopter Society 74th Forum, Phoenix, May 14-17, 2018.
[75] K. Richter, E. Schülein, B. Ewers, J. Raddatz, A. Klein, Boundary layer transition characteristics of a full-scale helicopter rotor in hover, American Helicopter Society 72nd Forum, West Palm Beach, May 17-19, 2016.
[76] U. Fey, Y. Egami, C. Tropea, A. Yarin, J.F. Foss (Eds.), "Transition Detection by Temperature-Sensitive Paint", Springer Handbook of Experimental Fluid Mechanics, Springer–Verlag, Berlin, 2007, pp. 537–552, , https://doi.org/10.1007/978-3-540-30299-5_7 Chap. 7.4.
[77] D. Yorita, K. Asai, C. Klein, U. Henne, S. Schaber, Transition detection on rotating propeller blades by means of temperature sensitive paint, 50th AIAA Aerospace Sciences Meeting. Grapevine, Texas, 9-12 January, 2012, https://doi.org/10.2514/6.2012-1187.
[78] M. Costantini, U. Fey, U. Henne, C. Klein, Nonadiabatic surface effects on transition measurements using temperature-sensitive paints, AIAA J. 53 (5) (2015) 1172–1187, https://doi.org/10.2514/1.J053155.
[79] J. Lemarechal, C. Klein, U. Henne, D.K. Puckert, U. Rist, Detection of Lambda- and Omega-vortices with the temperature-sensitive paint method in the late stage of controlled laminar-turbulent transition, Exp. Fluid 60 (6) (2019), https://doi.org/10.1007/s00348-019-2734-1.
[80] E. Gartenberg, A.S. Roberts, Airfoil transition and separation studies using an infrared imaging system, J. Aircr. 28 (4) (1991) 225–230, https://doi.org/10.2514/3.46016.
[81] M. Raffel, A.D. Gardner, T. Schwermer, C.B. Merz, A. Weiss, J. Braukmann, C.C. Wolf, Rotating blade stall maps measured by differential infrared thermography, AIAA J. 55 (5) (2017), https://doi.org/10.2514/1.J055452.
[82] M. Raffel, C.E. Willert, F. Scarano, C.J. Kähler, S.T. Wereley, J. Kompenhans, Particle Image Velocimetry: A Practical Guide, third ed., Springer, 978-3-319-68852-7, 2018, , https://doi.org/10.1007/978-3-319-68852-7.
[83] R.J. Adrian, J. Westerweel, Particle Image Velocimetry, Cambridge Univ. Press, Cambridge, England, U.K., 978-0521440080, 2011.
[84] M. Raffel, A. Bauknecht, M. Ramasamy, G.K. Yamauchi, J.T. Heineck, L.N. Jenkins, Contributions of particle image velocimetry to helicopter aerodynamics, AIAA J. 55 (9) (2017), https://doi.org/10.2514/1.J055571.
[85] K. Mulleners, M. Raffel, The onset of dynamic stall revisited, Exp. Fluid 52 (3) (2012) 779–793, https://doi.org/10.1007/s00348-011-1118-y.
[86] K. Mulleners, M. Raffel, Dynamic stall development, Exp. Fluid 54 (2) (2013), https://doi.org/10.1007/s00348-013-1469-7.
[87] B. Heine, K. Mulleners, G. Joubert, M. Raffel, Dynamic stall control by passive disturbance generators, AIAA J. 51 (9) (2013), https://doi.org/10.2514/1.J051525.
[88] S. Mariappan, A.D. Gardner, K. Richter, M. Raffel, Analysis of dynamic stall using dynamic mode decomposition technique, AIAA J. 52 (11) (2014) 2427–2439, https://doi.org/10.2514/1.J052858.
[89] C.C. Wolf, A.D. Gardner, C.B. Merz, S. Opitz, Influence of a back-flow flap on the dynamic stall flow topology, CEAS Aeronaut. J. 9 (2018) 39–51, https://doi.org/10.1007/s13272-017-0274-z.
[90] A. Le Pape, M. Costes, F. Richez, F. David, J.-M. Deluc, Experimental study of dynamic stall control using deployable leading-edge vortex generators, AIAA J. 50 (10) (2012) 2135–2145, https://doi.org/10.2514/1.J051452.
[91] M. Fuchiwaki, K. Tanaka, Vortex structure and scale on an unsteady airfoil, JSME Int. J. Ser. B Fluids Therm. Eng. 49 (4) (2006) 1056–1063, https://doi.org/10.1299/jsmeb.49.1056.
[92] V. Raghav, N. Komerath, Velocity measurements on a retreating blade in dynamic stall, Exp. Fluid 55 (2) (2014) 1–10, https://doi.org/10.1007/s00348-014-1669-9.
[93] V. Raghav, N. Komerath, Dynamic stall live cycle on a rotating blade in steady forward flight, J. Am. Helicopter Soc. 60 (3) (2015), https://doi.org/10.4050/JAHS.60.032007.
[94] D.M. Schatzman, A Study of Unsteady Turbulent Boundary Layer Separation under Conditions Relevant to Helicopter Aerodynamics, PhD Thesis University of Notre Dame, 2011.
[95] A. Zanotti, G. Gibertini, Experimental investigation of the dynamic stall phenomenon on a NACA 23012 oscillating airfoil", Proc. Inst. Mech. Eng. G J. Aerosp. Eng. 227 (9) (2012) 1375–1388, https://doi.org/10.1177/0954410012454100.
[96] F. De Gregorio, K. Pengel, K. Kindler, A comprehensive PIV measurement campaign on a fully equipped helicopter model, Exp. Fluid 53 (1) (2012) 37–49, https://doi.org/10.1007/s00348-011-1185-0.
[97] J. Rauleder, J.G. Leishman, Flow environment and organized turbulence structures near a plane below a rotor, AIAA J. 52 (1) (2014) 146–161, https://doi.org/10.2514/1.J052315.
[98] M.J. Bhagwat, M. Ramasamy, Effect of tip vortex aperiodicity on measurement uncertainty, Exp. Fluid 53 (5) (2012) 1191–1202, https://doi.org/10.1007/s00348-012-1348-7.
[99] J.T. Heineck, G.K. Yamauchi, A.J. Wadcock, L. Lourenco, Application of three-component PIV to a hovering rotor wake, American Helicopter Society 56th Forum, Virginia Beach, May 2-4, 2000.
[100] P.B. Martin, J.G. Leishman, G.J. Pugliese, S.L. Anderson, Stereoscopic PIV measurements in the wake of a hovering rotor, AHS 56th Forum, Virginia Beach, May 2-4, 2000.
[101] J.I. Milluzzo, J.G. Leishman, Vortical sheet behavior in the wake of a rotor in ground effect, AIAA J. 55 (1) (2017) 24–35, https://doi.org/10.2514/1.J054498.
[102] F. Richez, B. Ortun, Numerical investigation of the flow separation on a helicopter rotor in dynamic stall configuration, 42nd European Rotorcraft Forum. Lille, France, September 5-8, 2016.
[103] F. Richez, Numerical analysis of dynamic stall for different helicopter rotor flight conditions, AHS 73rd Forum, Fort Worth, Texas, May 9-11, 2017.

[104] R. Jain, Sensitivity study of high-fidelity hover predictions on the sikorsky S-76 rotor, J. Aircr. 55 (1) (2018) 78–88, https://doi.org/10.2514/1.C034076.
[105] N.M. Chaderjian, Navier-Stokes simulation of UH-60A rotor/wake interaction using adaptive mesh refinement, AHS 73rd Annual Forum, Fort Worth, May 9-11, 2017.
[106] M. Potsdam, H. Yeo, W. Johnson, Rotor airloads prediction using loose aerodynamic/structural coupling, J. Aircr. 43 (3) (2006) 732–742, https://doi.org/10.2514/1.14006.
[107] M. Potsdam, A. Datta, B. Jayaraman, Computational investigation and fundamental understanding of a slowed UH-60A rotor at high advance ratio, American Helicopter Society 68th Forum, Fort Worth, May 1-3, 2012.
[108] M. Raffel, U. Seelhorst, C. Willert, Vortical flow structures at a helicopter model measured by LDV and PIV, Aeronaut. J. 102 (1014) (1998) 221–228, https://doi.org/10.1017/S0001924000096391.
[109] P.B. Martin, G.J. Pugliese, J.G. Leishman, High resolution trailing vortex measurements in the wake of a hovering rotor, J. Am. Helicopter Soc. 48 (1) (2003) 39–52, https://doi.org/10.4050/JAHS.48.39.
[110] M. Ramasamy, J.G. Leishman, Benchmarking particle image velocimetry with laser Doppler velocimetry for rotor wake measurements, AIAA J. 45 (11) (2007) 2622–2633, https://doi.org/10.2514/1.28130.
[111] K. Kindler, K. Mulleners, H. Richard, B.G. van der Wall, M. Raffel, Aperiodicity in the near field of full-scale rotor blade tip vortices, Exp. Fluid 50 (6) (2011) 1601–1610, https://doi.org/10.1007/s00348-010-1016-8.
[112] M. Ramasamy, B. Johnson, T. Huismann, J.G. Leishman, Digital particle image velocimetry measurements of tip vortex characteristics using an improved aperiodicity correction, J. Am. Helicopter Soc. 54 (1) (2009), https://doi.org/10.4050/JAHS.54.012004.
[113] S.M. Mula, J.H. Stephenson, C.E. Tinnes, J. Sirohi, Dynamical characteristics of the tip vortex from a four-bladed rotor in hover, Exp. Fluid 54 (10) (2013), https://doi.org/10.1007/s00348-013-1600-9.
[114] J.N. Braukmann, T. Schwermer, C.C. Wolf, Investigation of young blade-tip vortices at a rotor test facility using stereoscopic PIV, Symposium of the German Association for Laser Anemometry GALA e.V., Karlsruhe, Germany, 2017.
[115] M. Raffel, K. Mulleners, K. Kindler, J.T. Heineck, Particle Image Velocimetry in helicopter aerodynamics: developments, challenges, and trends, American Helicopter Society 68th Forum, Fort Worth, Texas, May 1-3, 2012.
[116] A. Bauknecht, B. Ewers, O. Schneider, M. Raffel, Blade tip vortex measurements on actively twisted rotor blades, Exp. Fluid 58 (5) (2017), https://doi.org/10.1007/s00348-017-2312-3.
[117] A. Goerttler, J.N. Braukmann, T. Schwermer, A.D. Gardner, M. Raffel, Tip-vortex investigation on a rotating and pitching rotor blade, J. Aircr. 55 (5) (2018) 1792–1804, https://doi.org/10.2514/1.C034693.
[118] A. Goerttler, J.N. Braukmann, C.C. Wolf, A.D. Gardner, M. Raffel, Blade tip-vortices of a four-bladed rotor with axial inflow, Vertical Flight Society 75th Forum, Philadelphia, Pennsylvania, May 13-16, 2019.
[119] M. Raffel, H. Richard, K. Ehrenfried, B. Van der Wall, C. Burley, P. Beaumier, K. McAlister, K. Pengel, Recording and evaluation methods of PIV investigations on a helicopter rotor model, Exp. Fluid 36 (1) (2004) 146–156, https://doi.org/10.1007/s00348-003-0689-7.
[120] B.G. van der Wall, H. Richard, Analysis methodology for 3C-PIV data of rotary wing vortices, Exp. Fluid 40 (5) (2006) 798–812, https://doi.org/10.1007/s00348-006-0117-x.
[121] A.J. Wadcock, G.K. Yamauchi, E. Solis, A.E. Pete, PIV measurements in the wake of a full-scale rotor in forward flight, AIAA 29th Applied Aerodynamics Conference, Honolulu, Hawaii, 27-30 June, 2011, https://doi.org/10.2514/6.2011-3370.
[122] G.K. Yamauchi, A.J. Wadcock, W. Johnson, M. Ramasamy, Wind tunnel measurements of full-scale UH-60A rotor tip vortices, American Helicopter Society 68th Forum, Fort Worth, Texas, May 1-3, 2012.
[123] M. Potsdam, B. Jayaraman, UH-60A rotor tip vortex prediction and comparison to full-scale wind tunnel measurements, American Helicopter Society 70th Forum, Montreal, Quebec, May 20-22, 2014.
[124] R.T. Biedron, E.M. Lee-Rausch, Blade displacement predictions for the full-scale UH-60A airloads rotor, AHS 70th Forum, Montreal, May 20-22, 2014.
[125] C.C. Wolf, J.N. Braukmann, A. Bauknecht, M. Raffel, Elastic main rotor blade motions on whirl tower - Optical measurement technique, Deutscher Luft- und Raumfahrtkongress, Friedrichshafen, 4-6 Sept 2018.
[126] A. Bauknecht, M. Raffel, B. Grebing, Airborne acquisition of blade tip displacements and vortices on a coaxial helicopter, J. Aircr. 55 (5) (2018) 1995–2007, https://doi.org/10.2514/1.C034647.
[127] D. Schanz, S. Gesemann, A. Schröder, Shake-The-Box: Lagrangian particle tracking at high particle image densities, Exp. Fluid 57 (5) (2016), https://doi.org/10.1007/s00348-016-2157-1.
[128] C.C. Wolf, C. Schwarz, K. Kaufmann, A.D. Gardner, D. Michalis, J. Bosbach, D. Schanz, A. Schröder, Experimental study of secondary vortex structures in a rotor wake, 45th European Rotorcraft Forum, Warsaw, September 17-9, 2019.
[129] M. Raffel, Background-oriented schlieren (BOS) techniques, Exp. Fluid 56 (3) (2015), https://doi.org/10.1007/s00348-015-1927-5.
[130] M. Raffel, J.T. Heineck, E. Schairer, F. Leopold, K. Kindler, Background-oriented schlieren imaging for full-scale and in-flight testing, J. Am. Helicopter Soc. 59 (1) (2014), https://doi.org/10.4050/JAHS.59.012002.
[131] A. Bauknecht, C.B. Merz, M. Raffel, Airborne visualization of helicopter blade tip vortices, J. Vis. 20 (1) (2016) 139–150, https://doi.org/10.1007/s12650-016-0389-z.
[132] K. Kindler, E. Goldhahn, F. Leopold, M. Raffel, Recent developments in background oriented schlieren methods for rotor blade tip vortex measurements, Exp. Fluid 43 (2–3) (2007) 233–240, https://doi.org/10.1007/s00348-007-0328-9 Springer.
[133] A. Bauknecht, C.B. Merz, A. Landolt, A.H. Meier, M. Raffel, Blade-tip vortex detection in maneuvering flight using the Background-Oriented Schlieren technique, J. Aircr. 51 (6) (2014), https://doi.org/10.2514/1.C032672.
[134] A.H. Meier, T. Roesgen, Improved background oriented schlieren imaging using laser speckle illumination, Exp. Fluid 54 (6) (2013) 1549–1554, https://doi.org/10.1007/s00348-013-1549-8.
[135] C.C. Wolf, A.D. Gardner, B. Ewers, M. Raffel, Starting process of a pulsed jet as seen by schlieren measurements, AIAA J. 52 (8) (2014) 1821–1826, https://doi.org/10.2514/1.J053198.
[136] L. Venkatakrishnan, G.E.A. Meier, Density measurements using the background oriented schlieren technique, Exp. Fluid 37 (2) (2004) 237–247, https://doi.org/10.1007/s00348-004-0807-1.
[137] J.N. Braukmann, A. Bauknecht, C.C. Wolf, M. Raffel, "Towards density reconstruction of helicopter blade tip vortices from high-speed background oriented Schlieren data", New Results in Numerical and Experimental Fluid Mechanics XI, Notes Numer. Fluid Mech. Multidiscip. Des. 136 (2017) 375–385, https://doi.org/10.1007/978-3-319-64519-3_34.
[138] F. Klinge, M. Hecklau, M. Raffel, J. Kompenhans, U. Göhmann, Measurement of the position of rotor blade vortices generated by a helicopter in free flight by means of stereoscopic background oriented schlieren method (BOS), 13th Intl. Symp. On Applications of Laser Techniques to Fluid Mechanics, Lisbon, Portugal, 2006.
[139] J.T. Heineck, L.K. Kushner, E.T. Schairer, Measurements of tip vortices from a full-scale UH-60A rotor by retro-reflective background oriented schlieren and stereo photogrammetry, American Helicopter Society 69th Forum, Phoenix, May 21-23, 2013.
[140] A. Bauknecht, B. Ewers, C. Wolf, F. Leopold, J. Yin, M. Raffel, Three-dimensional reconstruction of helicopter blade-tip vortices using a multi-camera BOS system, Exp. Fluid 56 (1) (2015), https://doi.org/10.1007/s00348-014-1866-6.